



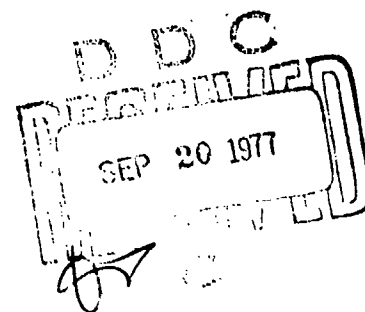
AD A045247

MATHEMATICAL MODEL OF FLIR PERFORMANCE

Paul M. Moser  
Aero Electronic Technology Department  
NAVAL AIR DEVELOPMENT CENTER  
Warminster, Pennsylvania 18974

19 October 1972

TECHNICAL MEMORANDUM  
AIRTASK NO. A3605333/202B/2F00343604



Approved for public release; distribution unlimited

AD NO. \_\_\_\_\_  
DDC FILE COPY.

Prepared for  
NAVAL AIR SYSTEMS COMMAND  
Department of the Navy  
Washington, D. C. 20360

UNCLASSIFIED

SECURITY CLASSIFICATION OF THIS PAGE (When Data Entered)

REPORT DOCUMENTATION PAGE		READ INSTRUCTIONS BEFORE COMPLETING FORM
1. REPORT NUMBER	2. GOVT ACCESSION NO.	3. RECIPIENT'S CATALOG NUMBER
4. TITLE (and Subtitle) MATHEMATICAL MODEL OF FLIR PERFORMANCE		5. TYPE OF REPORT & PERIOD COVERED Phase
7. AUTHOR(s) Paul M. Moser		6. PERFORMING ORG. REPORT NUMBER NADC-20203:PMM
9. PERFORMING ORGANIZATION NAME AND ADDRESS Aero Electronic Technology Department (Code 20) Naval Air Development Center Warminster, PA 18974		8. CONTRACT OR GRANT NUMBER(s) N1-20203-1-100
11. CONTROLLING OFFICE NAME AND ADDRESS Naval Air Systems Command Department of the Navy Washington, DC 20360		10. PROGRAM ELEMENT, PROJECT, TASK AREA & WORK UNIT NUMBERS P.E. 62753N Proj. No. F32-343 Task Area No. WF32-343-604
14. MONITORING AGENCY NAME & ADDRESS (if different from Controlling Office)		12. REPORT DATE 19 Oct 1972
		13. NUMBER OF PAGES 68
		15. SECURITY CLASS. (of this report) Unclassified
		15a. DECLASSIFICATION/DOWNGRADING SCHEDULE
16. DISTRIBUTION STATEMENT (of this Report) Approved for public release; distribution unlimited		
17. DISTRIBUTION STATEMENT (of the abstract entered in Block 20, if different from Report)		
18. SUPPLEMENTARY NOTES		
19. KEY WORDS (Continue on reverse side if necessary and identify by block number) Forward looking infrared; FLIR; infrared; passive infrared imaging; mathematical model; performance model; acquisition; classification; identification		
20. ABSTRACT (Continue on reverse side if necessary and identify by block number) In this technical memorandum a set of equations is developed which permits one to calculate acquisition, classification and identification ranges for ship targets when viewed by an airborne forward looking infrared (FLIR) imaging device. Inputs to the model are the average dimensions and aspect angle of the target, the average ship-to-background temperature difference, the surface air temperature and relative humidity, and the nominal resolution, noise equivalent temperature difference and altitude of the FLIR. Novel		

DD FORM 1 JAN 73 1473

EDITION OF 1 NOV 68 IS OBSOLETE

S/N 0102-LF-014-6601

UNCLASSIFIED

SECURITY CLASSIFICATION OF THIS PAGE (When Data Entered)

UNCLASSIFIED

SECURITY CLASSIFICATION OF THIS PAGE (When Data Entered)

features of the model are the use of square picture elements (pixels) to establish criteria for acquisition, classification and identification and the relating of pixel size to the minimum resolvable temperature difference of the FLIR.

Accession No. ☒ Section ☐  
Date ☐ Sub Section ☐  
Author ☐  
Title ☐  
Subject ☐  
Keywords ☐  
Abstract ☐  
Notes ☐  
References ☐  
Indexing ☐  
Classification ☐  
Distribution ☐  
Availability ☐  
Accession ☐  
Status ☐  
Remarks ☐  
A

S/N 0102- LF- 014- 6601

UNCLASSIFIED

SECURITY CLASSIFICATION OF THIS PAGE(When Data Entered)

NAVAL AIR DEVELOPMENT CENTER  
AERO ELECTRONIC TECHNOLOGY DEPARTMENT  
WARMINSTER, PENNSYLVANIA 18974

20203  
19 Oct 1972

TECHNICAL MEMORANDUM NADC-20203:PMM

Subj: Mathematical Model of FLIR Performance

Ref: (a)

- (b) T. L. Altshuler, "A Procedure for Calculation of Atmospheric Transmission of Infrared" General Electric Company Report No. R57ELC15 of 1 May 1957
- (c) Handbook of Chemistry and Physics, 37th edition, Chemical Rubber Publishing Company (1955)
- (d)
- (e) H. W. Yates and J. H. Taylor, Naval Research Laboratory Report 5453, "Infrared Transmission of the Atmosphere" of 8 Jun 1960
- (f) P. W. Kruse, L. D. McGlauchlin and R. B. McQuistan, Elements of Infrared Technology: Generation, Transmission, and Detection, John Wiley and Sons, Inc. (1962)
- (g) R. D. Hudson, Jr., Infrared System Engineering, John Wiley and Sons, Inc. (1960)
- (h) J. A. Hodges, "Infrared Image Test Program Study," Electro-Optical Systems, Inc./Air Force Avionics Laboratory Technical Report AFAL-TR-70-269 of Aug 1971
- (i)
- (j)
- (k) H. R. Blackwell, "Contrast Thresholds of the Human Eye," Journal of the Optical Society of America, Vol 46, No. 11 of Nov 1946, pp 624-643
- (l) J. Johnson, "Analysis of Image Forming Systems," Proceedings of the U.S. Army Engineer Research and Development Laboratories, Fort Belvoir, Va., Image Intensifier Symposium, 6-7 Oct 1958 (AD 220160) pp 249-273

- (m) R. V. Blackman (Editor), Jane's Fighting Ships, 1967-68 edition  
McGraw-Hill Book Company  
(n)

## I. BACKGROUND

Under AIRTASK A3605333/202B/2F00343604 NAVAIRDEVCECEN is performing operational and system analyses and state-of-the-art technology surveys and projections as a first effort in the development of FLIR (forward looking infrared) imaging devices which would be affordable in large quantities and optimized for the missions of single-place attack aircraft. In former years, FLIR imaging devices were selected usually on the basis of what was judged to be the "best" available, with high nominal spatial resolution serving as the principal criterion of what was "best." As a result FLIRs were applied to tasks for which their performance characteristics, in some cases, were quite inadequate and, in other cases, exceeded the real requirements. In both types of situation the results were not cost-effective.

The proximate purpose of these studies is to establish a framework in which one can serially relate fleet requirements, FLIR field performance, FLIR laboratory performance, FLIR design characteristics and FLIR cost in such a way that any one of these may be treated as an independent variable and the effects on the others observed. As a result of these investigations, one should be able to adjust the requirements imposed on a FLIR in such a way that its usable performance-to-cost ratio is optimized. In one of these studies, a probabilistic-type operational analysis is being performed which will indicate the variation in the number of ways an aircraft can make a successful attack as a function of the target identification range. In the study described in this technical memorandum, FLIR target acquisition, classification and identification ranges are related through laboratory-measurable performance quantities to FLIR design characteristics. In a third study, FLIR design characteristics are related to FLIR weight, complexity and cost.

The basic mathematical model described in this technical memorandum was developed during March and April 1971 and results obtained from exercising it were provided to the Naval Air Systems Command on 21 April 1971. The model was subsequently extended and generalized. Insofar as the application of this model may have far-reaching consequences with regard to the selection and procurement of FLIR equipments in large quantities, the desire was expressed from several quarters that the model be subjected to verification and, if necessary, correction and revision. The principal purpose in preparing this detailed description is to make the model available for criticism and verification.

## II. APPROACH

The acquisition, classification and identification of surface targets by means of airborne passive forward looking infrared imaging devices involves the following considerations: (1) the emission/reflection of radiant power from the target significantly different from that of the background; (2) the transmission of this power through the atmosphere; (3) the interception of a small fraction of this radiant power and the conversion of the signal information accompanying it into a visual image; and (4) the viewing and interpretation of the image by the FLIR observer. These factors will be considered in the establishment of a mathematical model of FLIR performance with particular emphasis on the acquisition, classification and identification of ships. A glossary of the symbols used in this memorandum is given in table I.

## III. EMISSION OF RADIATION FROM THE TARGET

In this discussion it is assumed that the targets and backgrounds behave as blackbody radiators. The spectral radiance  $\mathcal{Q}_\lambda$  of a blackbody can be calculated by use of Planck's radiation equation and is plotted in figure 1 over the wavelength interval of 3.0 to 15.0 micrometers for temperatures of 10°, 15° and 20°C. The peaks of these curves occur at a wavelength of about 10 micrometers.

In the interests of simplicity and of achieving a greater system effective dynamic range, most FLIRs respond only to radiant power variations rather than to the total power received by the individual detectors as they scan across the scene. This is done for two reasons. First, in practice, the FLIR operator observes targets by virtue of differences in (effective) temperature between the target and its background and by the spatial variation in (effective) temperature throughout the surface of the target rather than by sensing absolute temperatures. Second, in a typical scene, radiance differences are small compared with the total radiance; that is, radiance contrasts of less than 1.6% per Celsius degree are exhibited. Thus, of greater interest than the spectral radiance curves of figure 1 is the plot of the first partial derivative of the spectral radiance with respect to temperature  $\partial \mathcal{Q}_\lambda / \partial T$ , an example of which is shown in figure 2. The peak of this curve occurs at a wavelength between 8.0 and 9.0 micrometers. This curve is used in section VI to weight the atmospheric transmission curves.

## IV. TARGET-TO-BACKGROUND EFFECTIVE TEMPERATURE DIFFERENCE

A rigorous description of the effective thermal contrast between a target and its background is an extremely complicated undertaking even

for the apparently simple case of a ship against a sea-sky background. Effective radiation temperature measurements of a ship depend not only on the portion of the ship being examined but also on the angle of viewing, particularly in the case of a hot stack. These temperatures in turn are dependent upon variables such as the ship's power setting, heading relative to the wind and sun, sea state and weather history. Inasmuch as the sea surface does not radiate as an ideal blackbody and the reflectivity and emissivity of water vary as functions of angle, the background effective temperature depends upon the FLIR viewing angle, sea state and sky conditions. A much more detailed discussion of these variables is given in reference (a). In this technical memorandum it is assumed that the effective radiation temperatures of the target and of the background are uniform and independent of viewing angle and that at a given time and place the target-to-background temperature difference can be expressed by a single number. Representative ship-to-background temperature differences are of the order of several Celsius degrees.

#### V. TARGET EFFECTIVE PROJECTED AREA

The power radiated by a target is a function of its area. The effective projected area of a target depends upon its physical dimensions, the angle from which it is viewed and, if a ship, the amount by which it projects above the water line and/or the horizon. With regard to projected area and the manner in which it varies with viewing angle, it is assumed that the target shape can be approximated as a rectangular parallelepiped whose dimensions equal the average length, width and height of the target. Formulas are developed herein for two azimuthal viewing angles (beam aspect and bow/stern aspect) relative to the target and a continuum of elevation angles from 0 to 90°. This simple model of the target is somewhat complicated by the fact that the average dimensions of a ship sometimes depend upon the viewing direction. For example, because of the design of a ship's superstructure, its average height when viewed from the bow/stern angle is greater typically than its average height when viewed from the beam aspect. Accordingly, different rectangular parallelepiped models may be used for the two viewing directions of a particular ship.

If the target is beyond the horizon, its apparent height  $h'$  will be less than its actual height  $h$  above the water line as illustrated in figure 3. If it is assumed that the aircraft altitude  $p$  is very small compared to the earth's radius  $R_E$ , the slant range  $r_1$  to the horizon is given (in consistent units) by

$$\begin{aligned}
 r_1 &= \left[ (R_E + p)^2 - R_E^2 \right]^{1/2} = \left[ R_E^2 + 2 p R_E + p^2 - R_E^2 \right]^{1/2} \\
 &= (2 p R_E + p^2)^{1/2} \\
 &\approx (2 p R_E)^{1/2} .
 \end{aligned}$$

Similarly, the distance to the horizon from the lowest point on the target observable by the sensor is given (in consistent units) by

$$\begin{aligned}
 r_2 &= \left[ (R_E + h - h')^2 - R_E^2 \right]^{1/2} \\
 &\approx \left[ 2(h - h') R_E \right]^{1/2} .
 \end{aligned}$$

The range from the aircraft to the target (in consistent units)

$$r = r_1 + r_2 = (2 p R_E)^{1/2} + \left[ 2(h - h') R_E \right]^{1/2} .$$

Therefore

$$\left[ 2(h - h') R_E \right]^{1/2} = r - (2 p R_E)^{1/2}$$

and

$$2(h - h') R_E = r^2 - 2 r (2 p R_E)^{1/2} + 2 p R_E .$$



Thus the effective height of the target above the horizon (in consistent units)

$$h' = h - \frac{r^2}{2 R_E} + r \left[ \frac{2 p}{R_E} \right]^{1/2} - p.$$

This expression is valid only for the range interval for which the target is beyond the horizon but for which it has not completely disappeared beyond the horizon, i.e., for

$$(2 p R_E)^{1/2} < r < (2 R_E)^{1/2} (p^{1/2} + h^{1/2})$$

in which all quantities are expressed in consistent units.

If the radius of the earth  $R_E$  is taken as  $2.090 \times 10^7$  feet (3438 nautical miles) and if  $h'$ ,  $h$  and  $p$  are expressed in feet while  $r$  is expressed in nautical miles, the foregoing can be summarized as

$$h' = h - p + 1.880812 r p^{1/2} - 0.884364 r^2$$

$$\text{for } 1.06337 p^{1/2} < r < 1.06337 (p^{1/2} + h^{1/2}).$$

$$\text{For } r \leq 1.06337 p^{1/2}, h' = h. \quad \text{For } r \geq 1.06337 (p^{1/2} + h^{1/2}), h' = 0.$$

Figure 4 illustrates the geometry associated with the calculation of the effective projected area of the target when viewed by the FLIR from the beam aspect. The subscript 1 is used to denote the dimensions

of the target when viewed from the beam aspect. It is assumed that the sensor-to-target range is large in comparison with the dimensions of the target. The projected area of the ship in consistent units is

$$A_1 = l_1 (w_1 \sin \theta + h_1' \cos \theta).$$

$$\text{But } \sin \theta = \frac{p}{r}, \text{ and } \cos \theta = \frac{(r^2 - p^2)^{1/2}}{r}.$$

$$\text{Therefore } A_1 = \frac{l_1}{r} \left[ h_1' (r^2 - p^2)^{1/2} + w_1 p \right].$$

The formula for the projected area of the target viewed by the FLIR from the bow/stern aspect is similar except that the roles of  $l$  and  $w$  are interchanged and the subscript 2 is used to allow for the possibility that the target's average dimensions may vary with aspect angle. Thus

$$A_2 = \frac{w_2}{r} \left[ h_2' (r^2 - p^2)^{1/2} + l_2 p \right].$$

If the range  $r$  is expressed in nautical miles, the target dimensions in feet, and the projected target area in square feet, the foregoing two equations may be written as

$$A_1 = \frac{l_1}{6080 r} \left[ h_1' (3.697 \times 10^7 r^2 - p^2)^{1/2} + w_1 p \right] \text{ and}$$

$$A_2 = \frac{w_2}{6080 r} \left[ h_2' (3.697 \times 10^7 r^2 - p^2)^{1/2} + l_2 p \right].$$

Plots of these expressions showing the effective projected area of a destroyer as a function of range from an aircraft at various constant altitudes are given in figure 5.

## VI. ATMOSPHERIC TRANSMISSION

The attenuation by the intervening atmosphere of the infrared radiation emitted by the target and received by the sensor is one of the crucial factors involved in FLIR performance calculations. The principal molecular infrared absorbers in the atmosphere are water vapor, carbon dioxide and ozone. In addition, suspended particulate matter such as smoke, dust, and water droplets in the form of clouds, fog and haze scatter and absorb infrared radiation. Insofar as thick dense clouds and fog are opaque to infrared radiation, they will be considered no further in this discussion. Instead, an "average clear" atmosphere will be assumed. This assumption is not as serious as it would be for calculations in the visible part of the spectrum because visibility (except for the severe limitations imposed by clouds and fog) is usually governed by the distribution of particles suspended in the atmosphere which are large in size compared with the wavelengths of visible light but small compared with the infrared wavelengths of interest. Attempts to describe in mathematical models the effects of haze droplets on infrared transmission have been unsuccessful to date owing, it is believed, to the wide variation in the distributions of particle sizes encountered in the real world and of the difficulty of measuring these distributions. Accordingly, scattering and absorption by particulate matter in the atmosphere are not broken out as separate variables in this model but are included implicitly as constants in the data on attenuation by water vapor.

The concentration of ozone in the atmosphere is a function of altitude, latitude, time of year and weather conditions. On the average, the ozone in the atmosphere is concentrated predominantly in a layer which is centered at an altitude of about 79,000 feet. The concentration in this layer drops off to 10% of its peak value at about 28,000 feet. From data given in reference (b) it can be shown that at the relatively low altitudes at which FLIRs are operated, atmospheric transmission through ozone averages 96% over the 8.0- to 12.5-micrometer band for path lengths of 30 nautical miles. See figure 6. Absorption by ozone under these conditions is negligible in comparison with other losses.

Carbon dioxide, which is distributed quite uniformly throughout the atmosphere, is a strong absorber in certain bands of the infrared spectrum. However, in the 8.0- to 12.5-micrometer interval, the average transmission over a 30-nautical mile sea level path, calculated from data of reference (b), is 90%. See figure 7. In this band of interest, absorption by carbon dioxide is negligible in comparison with absorption by water vapor.

The most important and, unfortunately, the most variable atmospheric molecular absorber in the 8.0- to 12.5-micrometer band is water vapor. The water vapor concentration in the atmosphere, or absolute humidity, is a function of the air temperature and relative humidity and may vary from a few tenths of a gram per cubic meter in cold dry climates to as much as 50 grams per cubic meter in tropical jungle type climates.

The interrelation of relative humidity, absolute humidity and temperature can be seen in the following. In accordance with Dalton's law of partial pressures, the partial pressure  $P$  of the water vapor in a given volume  $V$  of air is equal to the pressure it would exert if it alone occupied the whole volume. Atmospheric water vapor may be regarded as a low density gas whose colligative properties are interrelated by the equation of state of an ideal gas

$$PV = \frac{m}{\gamma_m} R_u T_A$$

in which  $m$  is the mass of gas of molecular weight  $\gamma_m$  at an absolute temperature  $T_A$  occupying a volume  $V$  at a partial pressure  $P$  expressed in consistent units. The ratio  $m/\gamma_m$  gives the number of moles of gas and  $R_u$  is the universal gas constant which has a value of 8.314 joules/mole·K°. For water,  $\gamma_m = 18.02$  gm/mole. Thus, the absolute humidity

$$\frac{m}{V} = \frac{\gamma_m}{R_u} \frac{P}{T_A}$$

If  $m/V$  is to be expressed in gm/m<sup>3</sup> and  $P$  in mm of Hg, this equation converts to

$$\frac{m}{V} = 288.9 \frac{P}{T_A}$$

Values of the vapor pressure of water over liquid water taken from reference (c) were used in conjunction with the above equation to calculate the values of absolute humidity corresponding to saturated air (100% relative humidity) given in table II. This table expresses absolute humidities in two sets of units, namely "gm/m<sup>3</sup>" and "cm of precipitable water per nautical mile." The latter units, which are more convenient for calculating atmospheric transmission over long paths, are obtained by multiplying the values given in gm/m<sup>3</sup> by 0.1853 m<sup>3</sup>, the volume of a one nautical mile long

column of one square centimeter cross-sectional area, and expressing the resulting mass of water vapor in terms of the length of the column of liquid water it would produce if it were liquified. Since relative humidity is the ratio of the quantity of water vapor present to the quantity which saturates at a given temperature, absolute humidity and relative humidity are directly proportional at any given temperature. A family of curves interrelating these three variables is given in figure 8. If the relative humidity  $H_r$  is expressed in decimal form and the temperature  $T_A$  is given in  $^{\circ}\text{C}$ , the absolute humidity  $H_o$  at sea level expressed in centimeters of precipitable water per nautical mile is given by

$$H_o = H_r (0.912 + 5.731 \times 10^{-2} T_A + 1.760 \times 10^{-3} T_A^2 + 5.349 \times 10^{-5} T_A^3).$$

This empirical equation agrees with the data of table II within  $\pm 1.6\%$  for  $0^{\circ}\text{C} \leq T_A \leq 40^{\circ}\text{C}$  and  $0 \leq H_r \leq 1.00$ . (A simpler alternative but less precise empirical equation,  $H_o = 0.93 H_r e^{0.06 T_A}$  gives results within  $\pm 3.6\%$  for  $0^{\circ}\text{C} \leq T_A \leq 35^{\circ}\text{C}$ .)

The concentration of atmospheric water vapor varies as a function of altitude. Figure 9, which is taken from reference (d), gives average values for the concentration of water vapor as a function of altitude over eastern United States. To obtain average concentrations of water vapor over paths from the surface to various altitudes, the area under the curve was integrated from zero altitude to a number of different altitudes and the integrals divided by their respective altitude intervals. Table III is a summary of these average concentrations. The data of table III can be expressed by means of the empirical equation

$$H = 2.59 e^{-4.137 \times 10^{-5} p}$$

in which  $H$  is the average absolute humidity (in cm of precipitable water per nmi) over the interval from sea level to an altitude  $p$  (ft). Over the altitude range  $0 \leq p \leq 5000$  ft, this equation agrees with the data of table III within 0.7%; at an altitude of 8000 ft, there is a discrepancy of 6%; at 16,000 ft, the discrepancy is 8%.

If it is assumed that the average atmospheric water vapor concentration always varies with altitude in this same exponential manner, the preceding equation can be generalized as follows:

$$H = H_o e^{-4.137 \times 10^{-5} p} \quad \text{for } 0 \leq p \leq 16,000 \text{ ft}$$

in which  $H_o$  is the absolute humidity near sea level.

The total amount of water vapor  $W$  in a path of  $1 \text{ cm}^2$  cross-sectional area from the target to the sensor is then given by

$$W = H r$$

in which  $W$  is expressed in cm of precipitable water,  $H$  is in cm of precipitable water per nmi, and the range  $r$  is given in nautical miles.

The task of relating atmospheric transmission of infrared radiation to the total amount of water vapor in the path is addressed next. A review of the literature on the subject (e.g., references (b), (e), (f), (g) and (h)) reveals wide disparities in the values of transmission given. Data from these five references are plotted in figure 10 to illustrate this. Several criteria were applied in the selection of a single model of atmospheric transmission. First, transmission should equal 100% for zero path length and approach zero as the path length becomes very large. Second, data should be available for precipitable water column lengths up to 100 cm. Third, the available data must be in a conveniently usable form for calculations over the desired band (8.0 to 12.5  $\mu\text{m}$ ). Fourth, the data must agree with real-world experience. Fifth, the data should correspond roughly to the mean, as far as optimism is concerned, rather than the extremes. On these bases, the transmission models of references (h), (g), (e) and (f) were rejected in that order and the Altshuler model (reference (b)), which satisfied all the criteria, was adopted.

Figure 11 is a family of curves, adapted from Altshuler, giving the percent spectral transmission of infrared radiation through various length columns of precipitable water vapor at sea level. If the curve of figure 2 (the derivative of spectral radiance with respect to temperature) is multiplied point-by-point by each of the atmospheric transmission curves of figure 11, the family of curves shown in figure 12 results; the curve of figure 2 is also reproduced as a reference in figure 12. These curves show how the "signal" from a blackbody target differing in temperature by  $1.0\text{K}^\circ$  from its blackbody background varies in intensity and spectral content as the amount of water vapor in the path between the target and the sensor is varied. Note that the wavelength at which the maximum occurs shifts from about 8.6 micrometers to about 11.0 micrometers as the amount of water vapor in the path increases. The area under each of these eight curves was integrated over the selected spectral band of 8.0 to 12.5 micrometers; the values of these integrals are given in table IV. The data of table IV are plotted in figure 13.

For small values of temperature difference between a target and its background, the difference in target-to-background radiancy is directly proportional to the temperature difference if the emissivity  $\epsilon$  of the target and background are equal and constant; that is, since

$$Q = \sigma \epsilon T^4,$$

$$dQ = 4 \sigma \epsilon T^3 dT.$$

In these equations,  $\sigma$  is the Stefan-Boltzmann constant. Accordingly, the data plotted in figure 13 can be used to determine how the apparent target-to-background temperature difference varies as a function of the amount of water vapor in the path when the target is viewed by a remotely located FLIR if the target and the background are uniform and large compared to the ground resolution of the FLIR. This can be accomplished by normalizing the data of table IV to unity for the case of zero precipitable water vapor in the path as shown in table V and figure 14. For use in this mathematical model, it is more convenient to take the reciprocals of these apparent temperature differences (also given in table V and to express them as non-dimensional factors. The resulting data, which are plotted as a curve in figure 15, may be interpreted as the factor by which a target-to-background temperature difference must be multiplied when the target is viewed through a given amount of water vapor to produce the same intensity signal as would be produced under zero absorbing path conditions (laboratory conditions). For example, for two well-resolved targets to exhibit the same apparent thermal contrast on a FLIR, one viewed through 30 cm of precipitable water would have to possess an actual thermal contrast ten times greater than a similar one viewed under near-zero-range laboratory conditions. This "multiplier curve" can be represented by the empirical equation

$$M = 1.0625 + 0.19087 W + 7.9627 \times 10^{-4} W^2$$

$$+ 3.6011 \times 10^{-5} W^3 + 1.8868 \times 10^{-6} W^4$$

in which  $M$  is the multiplying factor described above and  $W$  is the length of the column of precipitable water in the target-to-sensor path. This equation agrees with the data points within  $\pm 6.3\%$  over the interval  $0 \leq W \leq 100$  cm of precipitable water.

## VII. SENSOR CHARACTERIZATION

In this technical memorandum, a method is developed for calculating FLIR classification and identification ranges by applying the concept of

MRT (minimum resolvable temperature difference) and for calculating acquisition ranges by applying the concept of MDT (minimum detectable temperature difference). The following assumptions are made:

1. The FLIR's response is uniform over the 8.0- to 12.5-micrometer band and zero outside of this band;
2. The FLIR scans and displays the scene uniformly and isotropically;
3. The total field of view of the FLIR is large in comparison with the target size;
4. The FLIR is pre-aimed at the target (perhaps by some other sensor) such that search is required only within the field of view of the sensor.

The concepts of MRT and MDT are based on the ability of observers to perceive, on the FLIR display, under laboratory conditions, images of "standard" temperature-controlled targets as their sizes and temperature difference relative to the background are varied. An operational definition of MRT is given in reference (1). To measure the MRT of a frame-scanning passive infrared imaging device, it is set up to view targets of the type illustrated in figure 16 in which the bars and the surround are blackbody radiators. If the narrow dimension of each bar in a set subtends as angle  $\gamma$  (in milliradians) at the sensor, the target spatial frequency  $f$  (in cycles per milliradian) is taken as

$$f = \frac{1}{2\gamma}.$$

The temperature difference between the bars and the surround is slowly increased from nearly zero until an operator viewing the display can barely resolve the largest set of bars. This temperature difference is defined as the MRT of the device at the spatial frequency of that particular set. The process is repeated for a series of similar targets of progressively smaller bar angular subtense  $\gamma$  and values of MRT obtained are plotted as a function of  $f$ . A representative MRT curve is plotted in figure 17. It should be noted that "resolution" and "sensitivity" are not independent constant quantities for a given FLIR but that one is a function of the other. FLIR "nominal resolution" should not be interpreted as "limiting resolution" insofar as bars smaller than the nominal resolution can be resolved, provided the bar-to-background temperature difference is sufficiently large. ("Nominal resolution," as



used here, is simply the ratio of the FLIR detector element dimension and the focal length of the FLIR optical system.) Furthermore, the FLIR noise equivalent temperature difference is not necessarily the smallest temperature difference that can be discerned on the FLIR display but rather a convenient, simple, objective quantity that is measured electronically.

Reference (1) provides measured MRT data for a number of infrared imaging devices having quite different design characteristics. If one multiplies the abscissae of each MRT plot by the nominal resolution  $\alpha$  of the particular equipment and divides the ordinates by its NET (noise equivalent temperature difference) one can plot the dimensionless ratio  $MRT(C^\circ)/NET(C^\circ)$  as a function of the dimensionless product  $f$  (cycles/mrad)  $\alpha$  (mrad). Figure 18 provides plots of MRT for six infrared imaging devices "normalized" in this manner. From these curves, a single, dimensionless, generalized, normalized MRT curve was drawn which is shown in figure 19 and which can be represented by the empirical expression

$$\frac{MRT}{NET} = 1.178 \times 10^{-3} e^{12.867 f \alpha + 3.32 f \alpha + 0.08}.$$

This equation, or the curve of figure 19, enables one to generate an MRT curve for any well-designed conventional FLIR, given only its nominal resolution and noise equivalent temperature difference. In a subsequent section, FLIR resolution and sensitivity requirements for the classification and identification of ships will be related to MRT.

Minimum detectable temperature difference is defined as that temperature difference which a uniform blackbody radiator subtending a solid angle  $\Omega$  (in microsteradians) at the FLIR sensor must exhibit to be barely detectable against a uniform blackbody background under laboratory (zero range) conditions. Reference (2) provides a theoretical treatment and derives an expression for the MDT of a current "typical good system" which, after recasting in the symbols of this technical memorandum, becomes

$$MDT = \frac{(\Omega + 4 \alpha^2) \alpha}{\Omega (\Omega + 6 \alpha^2)^{1/2}} NET.$$

The solid angle

$$\Omega = 10^6 A/r^2 \quad (\text{in consistent units}).$$

If one expresses the nominal resolution  $\alpha$  in milliradians, the range  $r$  in nautical miles, and the area  $A$  in square feet, the above two equations can be solved simultaneously to yield

$$\text{MDT} = \frac{6.08 \alpha r (A + 147.87 \alpha^2 r^2)}{A (A + 221.80 \alpha^2 r^2)^{1/2}} \text{ NET.}$$

This equation takes into account both spatial and temporal integration in the process of the observer's viewing the FLIR display and is based on experimental evidence that if the "perceived signal" is 1.8 times greater than the "perceived noise," the probability that the observer will detect the target, provided he looks at it, is 50%. When this equation is applied to a FLIR under field conditions, allowance must be made for atmospheric transmission losses; in such a situation one may interpret MDT as the minimum detectable apparent temperature difference. A plot of this equation applied to a representative FLIR ( $\alpha = 0.25$  mrad; NET =  $0.25^\circ\text{C}$ ) is given in figure 20. It is of interest to note that if the target exactly fills one nominal resolution element of the FLIR (i.e.,  $\Omega = \alpha^2$ ),  $\text{MDT} = 1.89 \text{ NET} = 0.47^\circ\text{C}$ . If 100 nominal resolution elements fall on the target (i.e.,  $\Omega = 100 \alpha^2$ ),  $\text{MDT} = 0.10 \text{ NET} = 0.025^\circ\text{C}$ . If the target is smaller than a nominal resolution element it can still be detected provided its temperature difference is sufficiently large; for example, a 0.1-mrad by 0.1-mrad ( $\Omega = 10^{-2}$  microsteradian) target can be detected by this representative 0.25-mrad FLIR provided the target-to-background temperature difference equals or exceeds  $2.62^\circ\text{C}$ .

The use of MDT to calculate the target-to-background temperature difference required to permit FLIR acquisition of a representative ship target is illustrated in the following example. The solid angle (in steradians) subtended by a target equals the effective projected area of the target divided by the square of its range. If the target area is given in square feet and the range in nautical miles,

$$\Omega = \frac{A}{3.697 \times 10^7 r^2}.$$

For a typical 9600-ft<sup>2</sup> destroyer viewed from the beam aspect at a range of 10 nautical miles

$$\Omega = \frac{9600}{3.697 \times 10^7 \times 100} = 2.60 \times 10^{-6} \text{ ster.}$$

At that range 41.6 nominal resolution elements from the 0.25-mrad FLIR fall on the target and the curve of figure 20 indicates that an apparent target-to-background temperature difference of  $0.04^{\circ}\text{C}$  is adequate for an observer, who knows exactly where to look on the display, to detect the target 50% of the time. If one sets the apparent target-to-background temperature difference at twice the MDT, the stimulus contrast may be assumed to have doubled and, in accordance with the findings of reference (k), the probability of detection is increased from 50% to 98%. One can now compensate for atmospheric transmission losses by utilizing the curves of figures 8 and 15. If, in the example, the air temperature is  $30^{\circ}\text{C}$  ( $86^{\circ}\text{F}$ ) and the relative humidity is 80%, the absolute humidity has a rather high value of 4.50 cm of precipitable water per nautical mile. For a range of 10 nautical miles, the length of the column is therefore 45 cm of precipitable water. The "multiplier" curve of figure 15 gives the value of the corresponding "temperature difference multiplier"  $M = 22$ . From the foregoing, one can arrive at the target-to-background temperature difference required for 98% probability of detection as

$$\Delta T = 2 \times (\text{MDT}) \times M = 2 \times 0.04 \times 22 = 1.8^{\circ}\text{C}.$$

If similar computations are performed for various other values of range, one can obtain corresponding sets of values of  $\Delta T$  and  $r$ . If  $r$  is plotted as a function of  $\Delta T$ , a curve is generated of which figure 21 is an example. If a likely value of the target-to-background temperature difference is  $4^{\circ}\text{C}$ , this curve yields an acquisition range of 12.4 nautical miles for the assumed set of conditions.

#### VIII. CRITERIA FOR TARGET CLASSIFICATION AND IDENTIFICATION

Whereas target acquisition involves as its only criterion the presentation of a signal on the FLIR display with an adequate combination of size and intensity to enable the observer to note with confidence that there is something of possible interest appearing on the display, target classification and identification involve the presentation of additional detailed information sufficient to categorize the target as falling into a particular group. It appears that during the run-in of an attack aircraft on a potential ship target, there are three decision points at which FLIR-generated information is relevant in determining the maneuvering of the aircraft. The first of these is the point at which acquisition of a potential target by the FLIR occurs; at this point the pilot may adjust his heading. As the aircraft approaches, target detail is gradually revealed until the second point is reached at which sufficient information is presented to enable the

observer to distinguish whether the target is a warship or a commercial ship. If it is a commercial ship, the pilot may break off his run and investigate other potential targets; if it is a warship, he may continue the run-in and make preliminary preparations for attacking. In this technical memorandum, classification is said to occur when a ship can be distinguished as a warship or a commercial ship. As the aircraft continues to approach, still more detail is revealed until the third point is reached at which the observer can distinguish the class of the ship such as a Forrest Sherman class destroyer or a Coontz class guided missile frigate. At this point he may commit his system to attack or break off the run. In this technical memorandum, identification is said to occur when the class of a ship can be distinguished.

Obviously, the quantitative expression of classification and identification criteria is an extremely complicated undertaking. Some of the factors involved are the attitude, skill and experience of the observer and the type of preflight briefing received. If, for example, the observer is told that there is only one ship in the area of interest and that it is a particular class of enemy ship, then acquisition is tantamount to identification. On the other hand, distinguishing a World War II liberty ship flying the American flag from a lend-lease vessel of the same type bearing a Soviet flag would be virtually impossible with a FLIR if the observer were told that some of each were in the same area. To illustrate the significance of experience in ship classification and identification, a particular Navy pilot, when given pictorial information of quality deemed inadequate even for classification, was able to identify a Buckley type destroyer escort. It was revealed later that he had served on that class of vessel for an extended period of time.

From the foregoing, it can be seen that the establishment of such criteria is fraught with great difficulty and that the results of range computations involving such criteria must be understood in the light of the original assumptions. Eventually, extensive psychophysical tests should be conducted to determine quantitative classification and identification criteria as a function of the type of vessel, similarity to other vessels in the test, viewing angle, and the observer's background, experience, attitude and briefing.

The most celebrated set of criteria is given by Johnson in reference (1) in which the quality of information presented in the image of the target and measures of the quality of information required for "detection," "orientation," "recognition," and "identification" are expressed in terms of resolvable line pairs per minimum critical target dimension. Average resolution requirements for performing each of these tasks against Army-type targets are given as 1.0, 1.4, 4.0 and 6.4 line

pairs respectively. These criteria seem to serve adequately provided there is no great disparity among the dimensions of a target; however, for ship-type targets the method breaks down. An example of this is shown in figure 22 which provides outline drawings of a particular class of destroyer from the bow and beam aspect angles. From one viewing angle the ratio of the average dimensions is 1.2 while from the other angle it is 14.6. It would be very difficult to identify the ship with certainty from the bow aspect drawing because the ship lacks distinguishing features when viewed from that angle; however, from the beam view, it is a straightforward matter to identify not only the class of this ship but also its particular modification. A brief examination of both drawings reveals that considerably more information is conveyed by the beam view than by the bow view. Yet if one were to view the ship with an imaging device sweeping out 40-inch wide scan "lines," 6.5 line pairs (adequate for "identification" according to the above criteria) would fit across the minimum average dimension of 43 feet for the bow aspect case whereas only 4.2 line pairs (adequate for "recognition") would fall across the minimum average dimension of 28 feet for the beam aspect case.

The difficulty discussed above can be circumvented if instead of counting the number of "lines" or bands falling on the target, one counts the number of resolvable squares or picture elements (pixels) falling on the target. If Johnson's criteria are applied to a hypothetical target of square projected area, then the number of picture elements required for detection, orientation, recognition and identification are 4.0, 7.8, 64 and 164 pixels, respectively. If this approach is now applied to the two views of the ship sketched in figure 22, the number of 40-inch square pixels falling on the beam view projected area is 1033 and the corresponding number for the bow aspect is only 194. These numbers convey a better idea of the relative information content provided by the two views of the ship than the relative number of line pairs previously given.

The basic assumption in the foregoing, that the amount of identifying information conveyed by a target image is a function of the projected area of the target, is one that is open to challenge. When applied to a ship, for example, the relatively featureless hull accounts for most of the projected area although most of the identifying information about the ship is conveyed through the details of the superstructure. Perhaps a better measure of information content would be the resolvable perimeter of the target or the number of resolvable angles along its perimeter. In either case, application of the criteria in a mathematical model would be a very difficult undertaking.

A second objection to the pixel approach (as used herein) is that it regards only the silhouette of the ship and does not take into account the possibility that details within the silhouette (such as the locations of warm engine areas) would contribute to its identification. This objection can be mitigated somewhat if infrared pictures of ships showing internal detail (instead of silhouettes) are used in arriving at numerical values for the number of pixels required to perform a given identification task.

Despite its shortcomings the pixel approach is used in this mathematical model. It can be shown that the pixel approach includes, as a special case, the "resolvable lines" approach which is applicable to targets whose linear dimensions along various axes are approximately equal. In addition, it covers long thin targets in a way that is at least qualitatively better than the resolvable lines approach. The pixel approach offers the additional advantages that it does not require specifying a critical dimension and it is readily adaptable for use in a mathematical model.

The next task is to determine the number of pixels required for classification and identification of ships. Ideally this should be done in a set of carefully controlled psychophysical tests involving various classes of observers who have been briefed in various ways and are viewing actual moving ships on an actual FLIR equipment aboard a moving aircraft. This has not been done. However, to gain some intuitive feeling for the amount of information required and to set up tentative criteria for classification and identification of ships, use was made of publications such as references (m) and (n) in which scale line drawings of ships viewed from the beam aspect angle are given. Some of these drawings were selected and covered with sheets of semi-transparent graph paper of various grid line spacings. If a given square block of the overlaid graph paper appeared to be at least fifty percent filled by a portion of the ship drawing, that block was blackened completely with ink; if a portion of the ship picture occupied less than fifty percent of a given block, that block was left blank. Examples of block-type silhouettes produced in this way are given in figure 23. In this case the original scale of the drawing is 150 feet/inch and 0.1-inch-block graph paper was used, thereby yielding a "ground resolution" of 15 feet. This corresponds roughly to a half milliradian at a range of five nautical miles. If these illustrations are viewed from a distance about 2000 times greater than the dimension of an individual block (16.7 feet in this case, which corresponds to a full scale range of five miles), the "blockiness" is no longer well resolved by the eye and the ship appears more realistic. Figure 23 demonstrates "quantizing" errors inherent in this approach. The blockiness mentioned above might be thought of as resulting from quantizing errors of size

and/or intensity; i.e., some features of the ship appear much more prominent than they should, whereas others may not appear at all. Other quantizing errors are errors of position which depend upon how the block matrix happens to fall on the ship drawing. Figure 23(a) is a silhouette produced from the original drawing in the reference; figure 23(b) is the first block silhouette made from the original drawing; figures 23(c), 23(d), and 23(e) show how the block silhouettes vary if the grid pattern is displaced approximately a half-block dimension vertically, horizontally and a combination of horizontally and vertically, respectively.

Figures 24 through 31 provide block-type silhouettes of various commercial vessels and, as references, silhouettes derived from graphic profiles given in reference (n). The scale of each of the original pictures was 131 feet per inch and block sizes of  $1/4$ ,  $1/8$  and  $1/10$  inch were chosen to yield ground resolutions of 32.8, 16.4 and 13.1 feet respectively, which correspond to angular resolutions of 1.1, 0.54 and 0.43 milliradian respectively at a range of five nautical miles. The types of ships illustrated are a small passenger ship, a small tanker, a freighter, a liberty ship, and four cargo vessels. The number of pixels falling on the ship in each case and the number of right angles in the block silhouettes are indicated on the figures. The general profile of each ship becomes apparent as the number of pixels falling on it equals 60 to 70.

Figures 32 through 35 provide block-type silhouettes and graphic profile silhouettes of two pairs of warships, the cruisers Baltimore and Sverdlov and the destroyers Forrest Sherman and Kotlin. In these cases, the original scale was 150 feet per inch and seven different block sizes,  $1/4$ ,  $1/8$ ,  $1/10$ ,  $1/12$ ,  $1/16$ ,  $1/20$  and  $1/25.4$  inch were chosen to yield ground resolutions of 37.5, 18.8, 15.0, 12.5, 9.4, 7.5 and 5.9 feet, respectively. These correspond to angular resolutions of 1.2, 0.62, 0.49, 0.41, 0.31, 0.25 and 0.19 milliradian, respectively, at a range of five nautical miles. Once again, to provide increased realism, the blockiness of the silhouettes may be reduced to a negligible level by viewing them at distances of about 2000 times the block dimensions; namely, 42, 21, 17, 14, 10, 8.3 and 6.6 feet. If the silhouettes are viewed by the unaided eye at these distances under average office illumination, the level of detail is comparable to what one would achieve with a 0.5-milliradian equipment viewing the full scale ship with a very high signal-to-noise ratio at ranges of 12, 6.2, 4.9, 4.1, 3.1, 2.5 and 1.9 nautical miles, respectively. The optimum distances for viewing the block silhouettes -- that is, the compromise distance at which most of the relevant details of the

pictures are observable but their blockiness is not a strong distracting influence -- is that at which the blocks subtend at the eye an angle of about one milliradian or about half the values given above; that is, 21, 10, 8.3, 6.9, 5.2, 4.2 and 3.3 feet, respectively.

The warship silhouettes of figures 32 through 35 should be compared with the commercial vessel silhouettes of figures 24 through 31. It is seen that as the number of pixels per ship increases, the characteristic features of the warships (e.g., their typical "triangular" appearance) and of the commercial vessels gradually evolve until one is able to distinguish the two types. Although systematic experiments have not yet been conducted to determine the probability of correct "classification" of a ship as a function of the pixel number, it appears that 60 to 70 pixels per ship are adequate to distinguish warships from commercial ships with a high probability of being correct.

Attention is now directed toward criteria for ship "identification." The two pairs of warships shown in figures 32 through 35 were selected because of their similarity and because one might be required to distinguish them in the event of conflict. If one compares figure 32 with 33 and figure 34 with 35, it appears that sufficient identifying detail is revealed when the pixel number is of the order of 400. Although systematic experiments have not yet been performed to establish identification criteria in terms of the pixel number, applying this tentative criterion to beam aspect views of ships yields results which are consistent with Johnson's criterion for identification. To illustrate, if one examines the block silhouettes of the Kotlin and Forrest Sherman classes of destroyers corresponding to 367 and 357 pixels, respectively, one observes that they may be regarded as being covered by about 13 horizontal "scan lines," which agrees with Johnson's criterion of 6.4 line pairs being required for identification. One of the deficiencies of Johnson's approach, which the pixel approach avoids, is the somewhat arbitrary selection of a "minimum critical dimension" for the target.

The task now remains to relate the pixel sizes required for classification and identification of any given target to the spatial frequency associated with those pixels at any given range and viewing direction and to relate the required spatial frequency to the required target-to-background temperature difference by means of the sensor MRT curve or equation. This is accomplished in part by equating the angular dimension of the required size pixel to the angular width of a single bar of the target array used to measure system MRT. If  $n$  is taken as the number of pixels required to fall upon the target to permit classification or identification and if, as before,  $\Omega$  is the solid angle (in microsteradians)



subtended by the target at the sensor, then the angular dimension (in milliradians) subtended by each pixel is given by

$$\gamma = \left( \frac{n}{n} \right)^{1/2}$$

Here the same symbol  $\gamma$  is used to denote pixel angular subtense as was used previously to denote the angular subtense of a single bar of an MRT test pattern. Therefore, the spatial frequency (in cycles/milliradian) required to permit classification or identification is

$$f = \frac{1}{2\gamma} = \frac{1}{2} \left( \frac{n}{n} \right)^{1/2} = \frac{1}{2} \left( \frac{n r^2}{10^6 A} \right)^{1/2} = \frac{r}{2000} \left( \frac{n}{A} \right)^{1/2}$$

in which, as before,  $r$  is the target-to-sensor range and  $A$  is the effective projected target area (in consistent units). If the range is expressed in nautical miles and the target area in square feet, this equation becomes

$$f = 3.04 r (n/A)^{1/2}.$$

From this equation it is seen that the spatial frequency to which the FLIR sensor must respond increases with target range and the amount of detailed information required to perform the intended task of classification or identification. In addition, the smaller the target, the higher the spatial frequency response that is required.

In the foregoing, it is tacitly assumed that the target can be likened to the standard four-bar MRT test pattern. In the case of a ship, the key point involved in its classification/identification is the degree to which the superstructure is resolved. If one reexamines the ship silhouettes of figures 23 through 35, one can regard their superstructures as consisting of vertical bars (which must be resolved) not too unlike the vertical bars of the MRT test pattern in their length-to-width ratios and in the number of cycles.

For a given FLIR to resolve the detailed structure of a particular target at a particular range, it must respond to the target spatial frequency, and its MRT at that spatial frequency must be smaller than the target-to-background temperature difference multiplied by the weighted atmospheric transmission. Because MRT is defined in terms of temperature

differences that enable an operator barely to resolve the bars of the test target, corresponding roughly to 50% probability of discerning the bars, the temperature difference required in this model for target classification and identification has been increased by a factor of two to increase this probability to approximately 98%.

The procedure for calculating target-to-background temperature differences required for classification and identification is similar to that previously described for target acquisition. The effective projected area of the target is first determined by inserting the target's dimensions and slant range and the sensor's altitude into the equations developed in section V. This target area, the slant range, and the number of pixels selected as a criterion for classification/identification are then used to calculate the spatial frequency required to perform the task. (In exercising this model, values of  $n = 66$  and  $n = 400$  have been used as criteria for classification and identification, respectively.) The FLIR MRT at that spatial frequency is then determined either from the measured MRT curve of the particular equipment or from the generalized MRT equation given in section VII. The resulting MRT value is then multiplied by two and by the atmospheric attenuation "multiplier"  $M$  developed in section VI to yield the required target-to-background temperature difference  $\Delta T$ . If similar computations are performed for various values of the slant range  $r$ , the resulting sets of numbers can be plotted as a curve of classification/identification range as a function of  $\Delta T$ . Examples of such curves are given in figure 36. For a reasonable target-to-background temperature difference of  $40^\circ$ , these curves yield classification and identification ranges of 7.2 and 3.8 miles, respectively, for a 400-foot long destroyer under the assumed conditions.

It should be made clear that, effectively, the number of pixels falling on the target is not determined simply by the geometrical projection of nominal resolution elements onto the target but rather by the projection of truly resolvable elements whose size depends upon the apparent target-to-background temperature difference. That is, the effective resolution depends not only on the design and construction characteristics of the FLIR but also on the target-to-background temperature difference and the atmospheric transmission. Stated differently, FLIR resolution is dependent upon the signal-to-noise ratio in any given situation. The foregoing is accomplished in this model by the use of MRT. For example, if one refers again to the MRT curve of a representative FLIR ( $\alpha = 0.25$  mrad;  $NET = 0.250^\circ$ ) given in figure 17 and if one multiplies the plotted MRT values by the factor of two previously discussed, it is seen that if the apparent target-to-background temperature difference is  $2.00^\circ$ , the angle subtended by each pixel dimension is 0.22 mrad whereas if the apparent target-to-background temperature difference is only  $0.50^\circ$ , the angle subtended by each pixel increases to 0.47 mrad.

## IX. CONCLUSION

The various substructures developed in the preceding sections may now be incorporated into an integrated mathematical model of FLIR performance. The key equations and inequalities are summarized in figure 37. A modular form is used to simplify computer programming, to make it possible to delete or investigate separately certain portions of the model, and to permit its further growth, modification and refinement. Data generated by exercising this model will be given in a subsequent technical memorandum.

## X. ACKNOWLEDGEMENT

The author wishes to express appreciation to Miss Nancy MacMeekin, who provided valuable assistance in the selection and preparation of the ship silhouettes, to Mrs. Rosalie Garofalo, who painstakingly typed the manuscript, and to Miss Ann Gana, who typed the figure legends.

*Paul M. Moser*

PAUL M. MOSER

TABLE I  
GLOSSARY OF SYMBOLS

<u>Symbol</u>	<u>Description</u>	<u>Units</u>
A	Effective projected area of target	ft <sup>2</sup>
A <sub>1</sub>	Effective projected area of target when viewed from beam aspect	ft <sup>2</sup>
A <sub>2</sub>	Effective projected area of target when viewed from bow or stern aspect	ft <sup>2</sup>
e	Base of the Napierian system of logarithms	dimensionless
f	Target spatial frequency	cycles/mrad
H	Absolute humidity	cm of precipitable water per nmi
H <sub>c</sub>	Absolute humidity near sea level	cm of precipitable water per nmi
H <sub>r</sub>	Relative humidity (expressed in decimal form)	dimensionless
h	Average height of target above the water line	ft
h'	Average height of target above the horizon	ft
h <sub>1</sub>	Average height of target above water line when viewed from beam aspect	ft
h' <sub>1</sub>	Average height of target above horizon when viewed from the beam aspect	ft
h <sub>2</sub>	Average height of target above water line when viewed from bow aspect	ft
h' <sub>2</sub>	Average height of target above horizon when viewed from the bow aspect	ft
l <sub>1</sub>	Average length of target above the water line when viewed from beam aspect	ft

TABLE I (cont'd)

<u>Symbol</u>	<u>Description</u>	<u>Units</u>
$l_2$	Average length of target when observed in plan view	ft
M	Multiplying factor to compensate for atmospheric transmission loss	dimensionless
m	Mass of water vapor	gm
$m$	Molar mass (molecular weight) of water	gm/mole
MDT	Minimum detectable temperature difference	C°
MRT	Minimum resolvable temperature difference	C°
MT	Minimum temperature difference	C°
n	Number of pixels required for classification or identification	dimensionless
NET	Noise equivalent temperature difference	C°
P	Partial pressure of water vapor in the air	mm of Hg
p	Sensor altitude	ft
$R_E$	Radius of the earth	ft
$R_u$	Universal gas constant	joule(mole·K°) <sup>-1</sup>
r	Slant range from sensor to target	nmi
$r_1$	Slant range from sensor to horizon	nmi
$r_2$	Slant range from target to horizon	nmi
$\mathcal{Q}$	Radiancy	watt cm <sup>-2</sup>
$\mathcal{Q}_\lambda$	Spectral radiance	watt cm <sup>-2</sup> $\mu\text{m}^{-1}$
T	Temperature of target or background	°C, °K

TABLE I (cont'd)

<u>Symbol</u>	<u>Description</u>	<u>Units</u>
$\Delta T$	Temperature difference between target and background	$^{\circ}\text{C}, ^{\circ}\text{K}$
$T_A$	Air temperature	$^{\circ}\text{C}, ^{\circ}\text{K}$
$V$	Volume of air	$\text{m}^3$
$W$	Total precipitable water in sensor-to-target path	cm of precipitable water
$w_1$	Average width of target when observed in plan view	ft
$w_2$	Average width of target above water line when viewed from bow aspect	ft
$\alpha$	Nominal resolution	mrad
$\gamma$	Angle subtended at sensor by small dimension of each bar of MRT target	mrad
$\epsilon$	Emissivity	dimensionless
$\theta$	Depression angle from which target is viewed	radians
$\lambda$	Wavelength	$\mu\text{m}$
$\sigma$	Stefan-Boltzmann constant	$\text{watt cm}^{-2} (\text{K}^{\circ})^{-4}$
$\tau_{\lambda}$	Atmospheric spectral transmission	dimensionless
$\Omega$	Solid angle subtended at sensor by target	microsteradians

TABLE II  
WATER VAPOR CONTENT OF SATURATED AIR AS A FUNCTION OF TEMPERATURE

Temperature (°C)	Temperature (°K)	Vapor Pressure of Water (mm of Hg)	Absolute Humidity (gm/m <sup>3</sup> )	Absolute Humidity (cm of precipitable water per nmi)
-15	258.2	1.436	1.607	0.2978
-10	263.2	2.149	2.359	0.4371
-5	268.2	3.163	3.407	0.6313
0	273.2	4.579	4.842	0.8972
5	278.2	6.543	6.795	1.259
10	283.2	9.209	9.394	1.741
15	288.2	12.788	12.82	2.375
20	293.2	17.535	17.28	3.202
25	298.2	23.756	23.02	4.265
30	303.2	31.824	30.32	5.619
35	308.2	42.175	39.53	7.326
40	313.2	55.324	51.03	9.456

TABLE III

AVERAGE WATER VAPOR CONCENTRATION OVER  
CERTAIN ALTITUDE INTERVALS FOR EASTERN UNITED STATES

Altitude Interval (feet)	Average Water Vapor Concentration	
	(gm/m <sup>3</sup> )	(cm of precip. water/nmi)
0-0	14.00	2.59
0-500	13.75	2.55
0-1000	13.45	2.49
0-2000	12.95	2.40
0-4000	11.93	2.21
0-8000	9.45	1.75
0-16,000	6.66	1.23
0-32,000	3.78	0.70



TABLE IV

DIFFERENCE IN RADIANCE OF A 15°C BLACKBODY PER KELVIN DEGREE  
DIFFERENCE IN TEMPERATURE TRANSMITTED THROUGH PRECIPITABLE  
WATER AT SEA LEVEL INTEGRATED OVER THE WAVELENGTH INTERVAL  
 $8.0 \mu\text{m} \leq \lambda \leq 12.5 \mu\text{m}$

Precipitable Water Vapor in Path (cm)	Apparent Radiance Difference ( $\text{watt cm}^{-2} (\text{K}^\circ)^{-1}$ )
0	$202.2 \times 10^{-6}$
1	$154.5 \times 10^{-6}$
2	$136.6 \times 10^{-6}$
5	$99.8 \times 10^{-6}$
10	$65.4 \times 10^{-6}$
20	$34.9 \times 10^{-6}$
50	$7.0 \times 10^{-6}$
100	$0.8 \times 10^{-6}$

TABLE V

APPARENT TARGET-TO-BACKGROUND TEMPERATURE DIFFERENCE FOR AN  
EXTENDED AREA BLACKBODY DIFFERING IN TEMPERATURE FROM ITS  
BACKGROUND BY  $1\text{C}^\circ$  AS A FUNCTION OF THE AMOUNT OF WATER VAPOR  
IN THE PATH BETWEEN TARGET AND SENSOR

Precipitable Water Vapor in Path (cm)	Apparent Temperature Difference ( $\text{C}^\circ$ )	Reciprocal of Apparent Temperature Difference ( $(\text{C}^\circ)^{-1}$ )
0	1.000	1.000
1	0.764	1.309
2	0.676	1.480
5	0.494	2.026
10	0.323	3.092
20	0.173	5.794
50	0.0346	28.89
100	0.00396	252.8

FIGURE 1. SPECTRAL RADIANCE OF A BLACKBODY

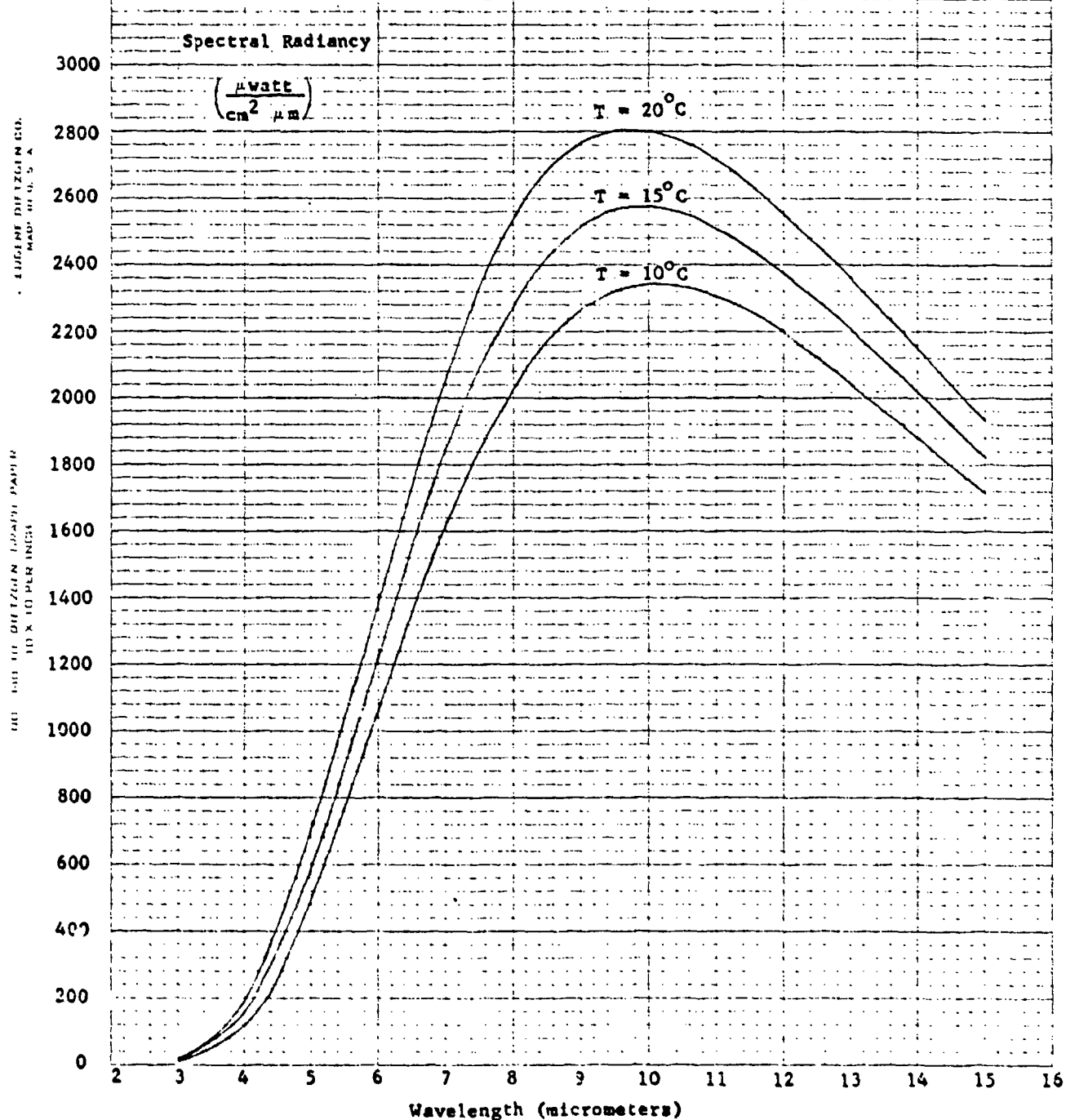
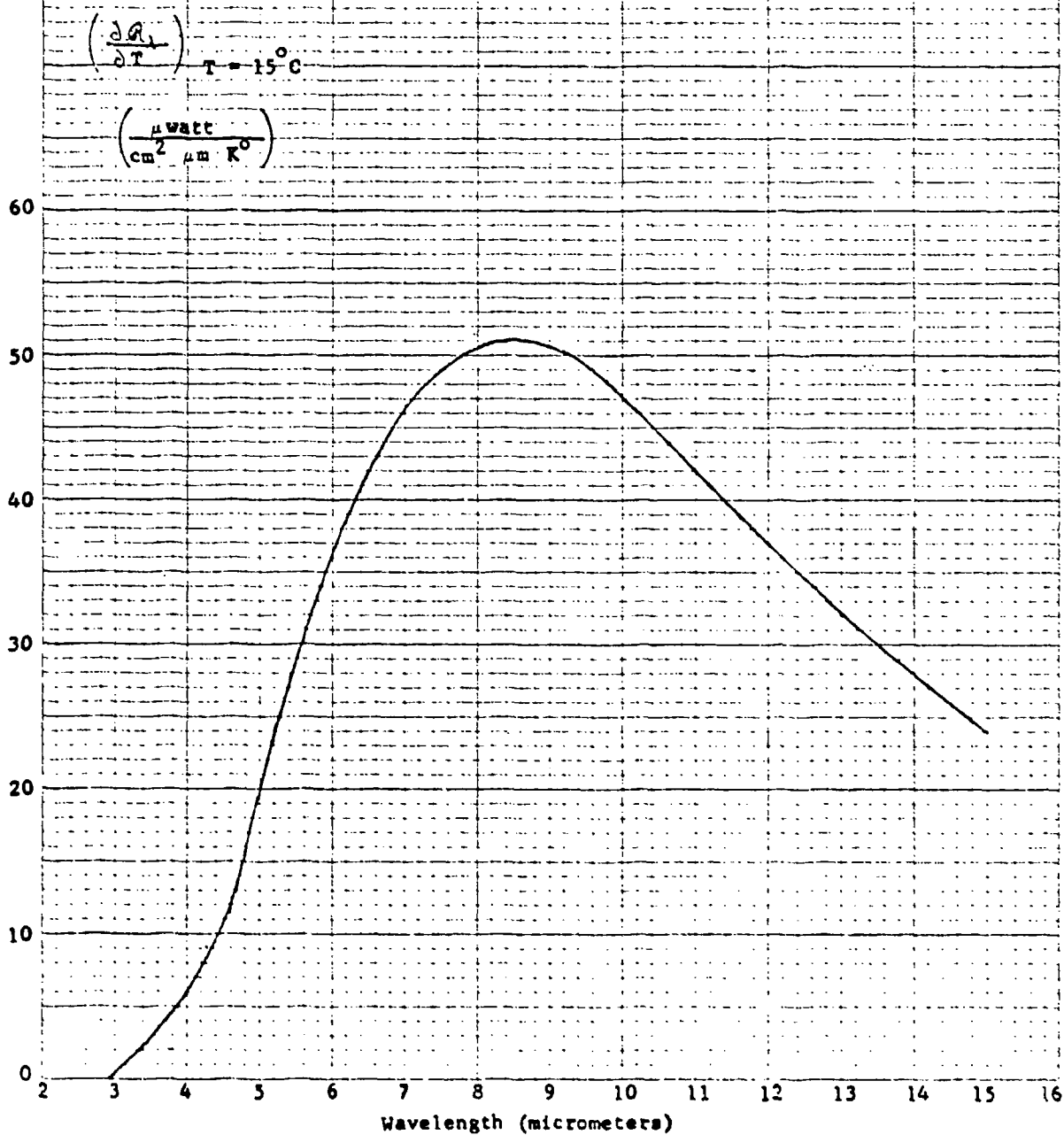


FIGURE 2. FIRST PARTIAL DERIVATIVE OF THE SPECTRAL RADIANCE  
OF A 15°C BLACKBODY WITH RESPECT TO TEMPERATURE

EUGENE DITZGEN CO.  
MADE IN U. S. A.

NO. 213 TO DITZGEN GRAPH PAPER  
10 X 10 PER INCH



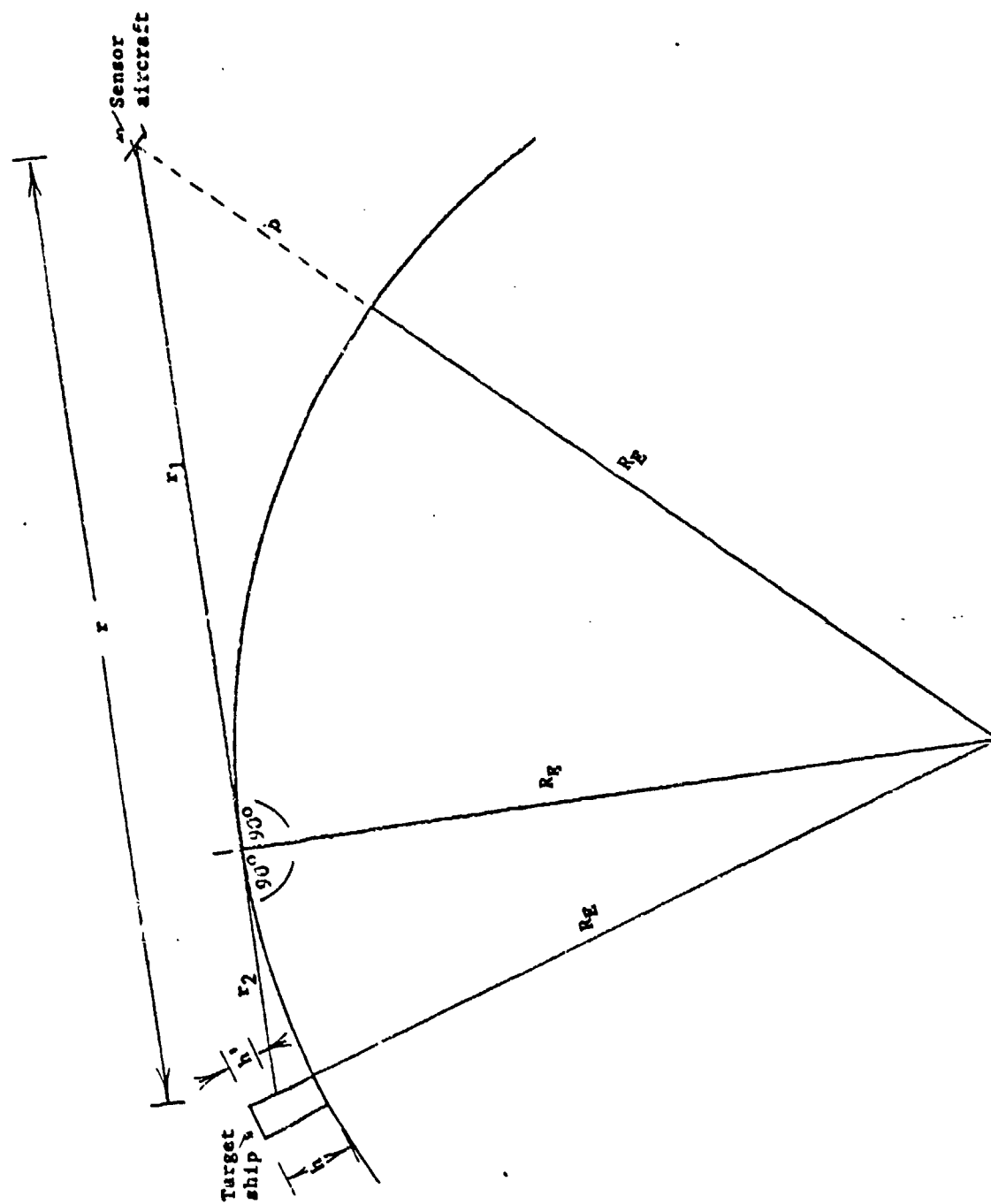
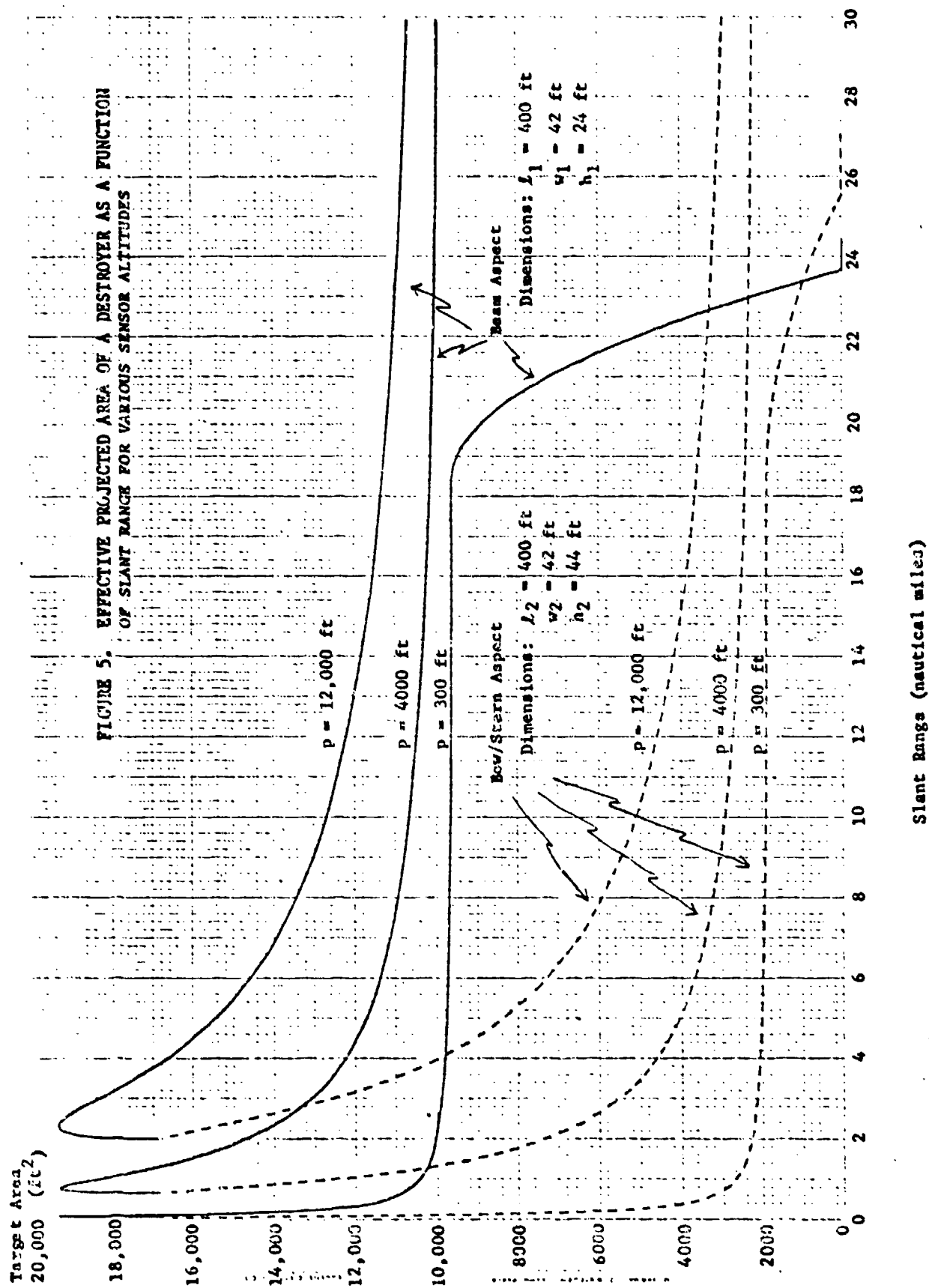


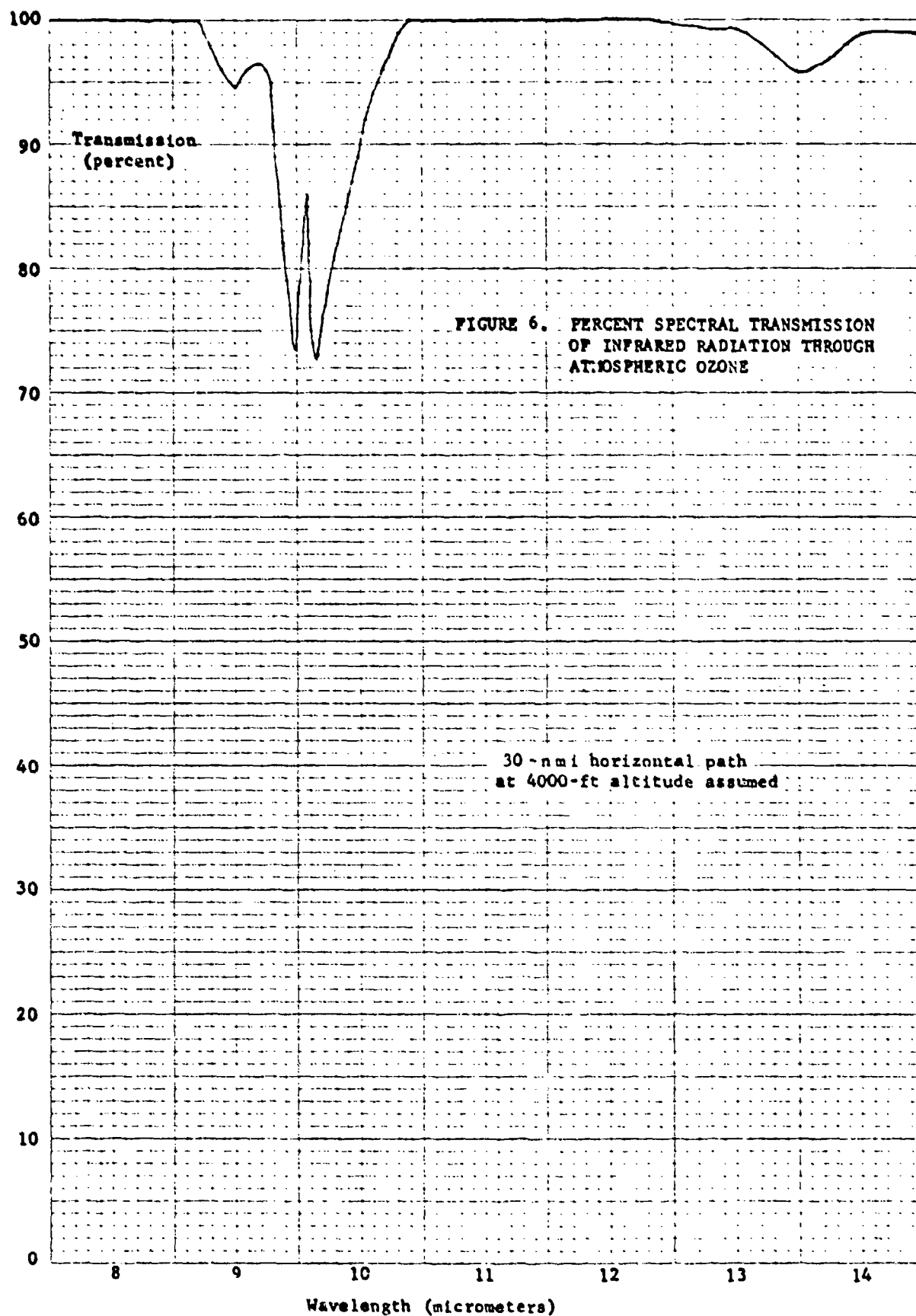
FIGURE 3. EFFECT OF EARTH'S CURVATURE ON THE APPARENT HEIGHT OF SHIP TARGET





ENCLOSURE FOR FIGURE 6  
MADE IN U. S. A.

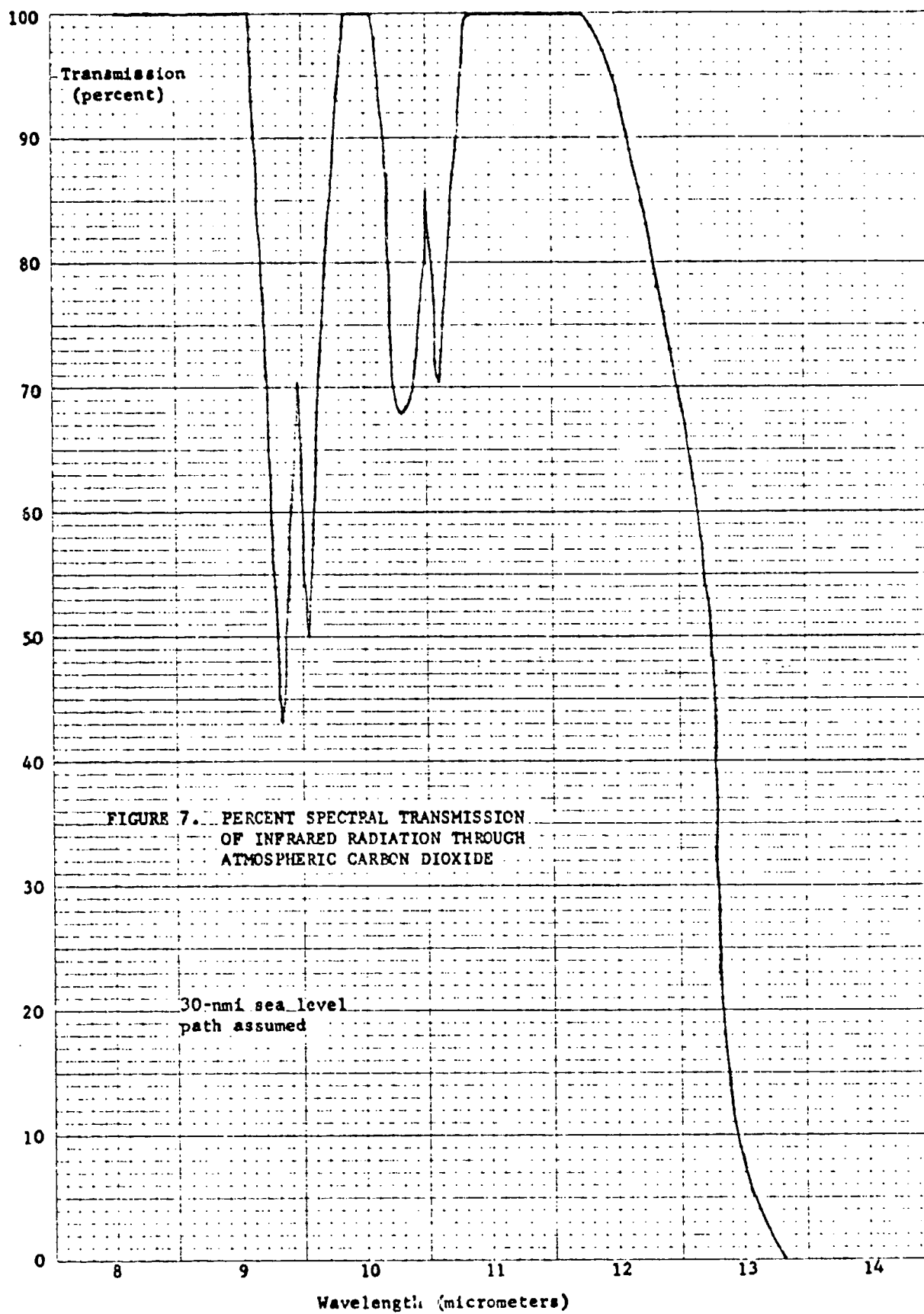
10 X 10 PER INCH

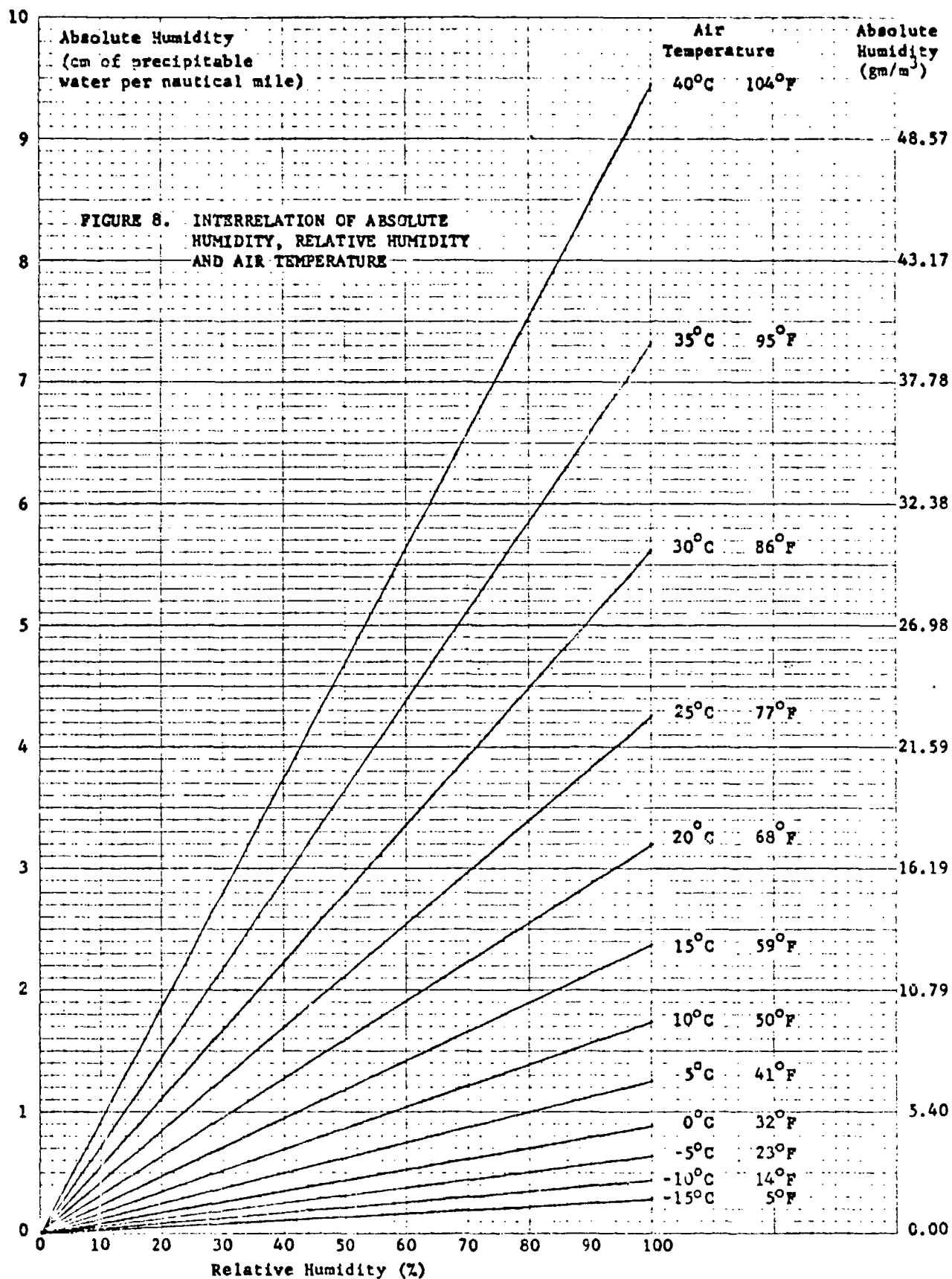




EUGENE DIEZGEN CO.  
MADE IN U. S. A.

NO. 3411 10" DIEZGEN GRAPH PAPER  
10 X 10 PER INCH

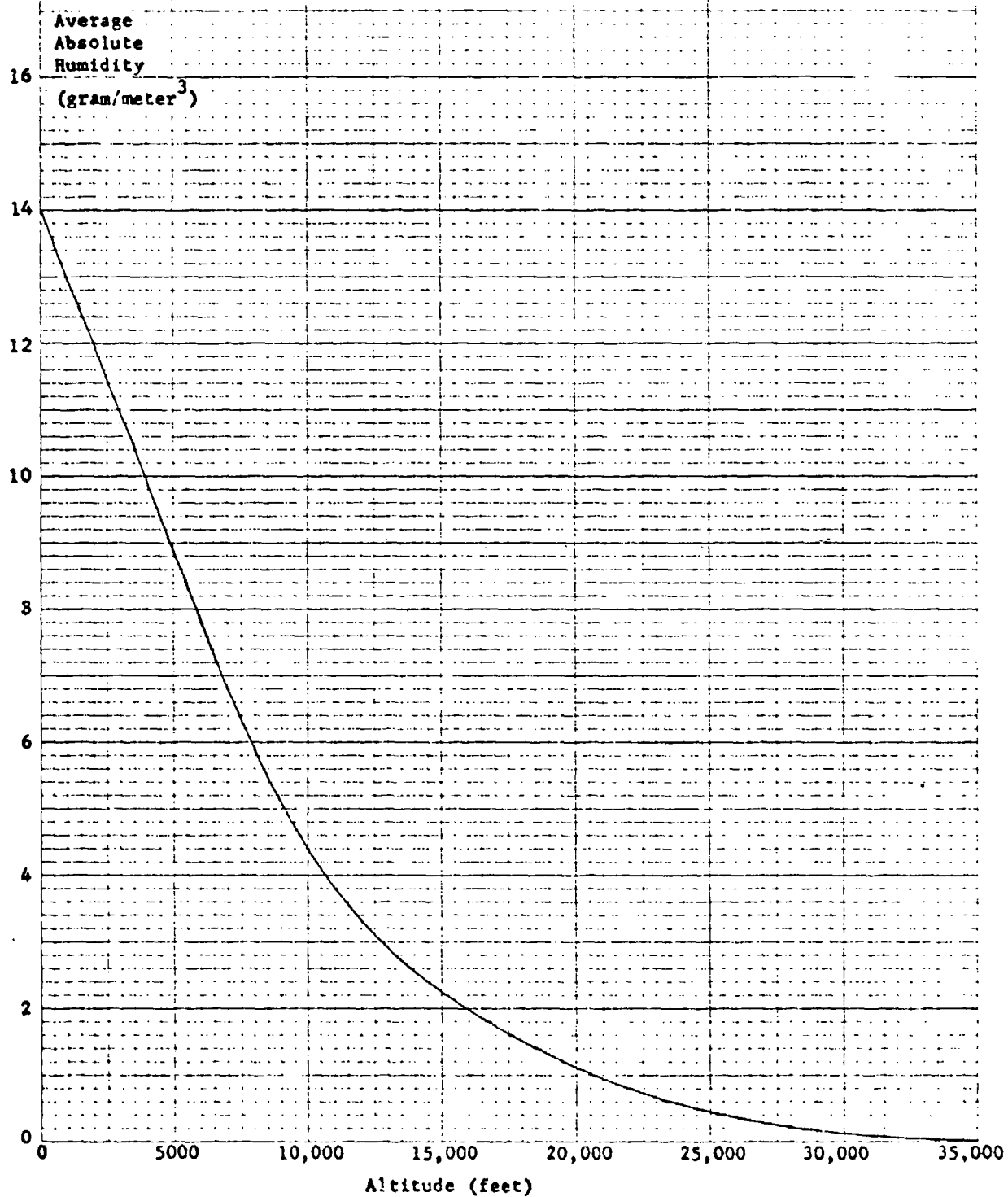




EUGENE DIFTZGEN CO.  
MADE IN U. S. A.

NO. 340-10 DIFTZGEN GRAPH PAPER  
10 X 10 PER INCH

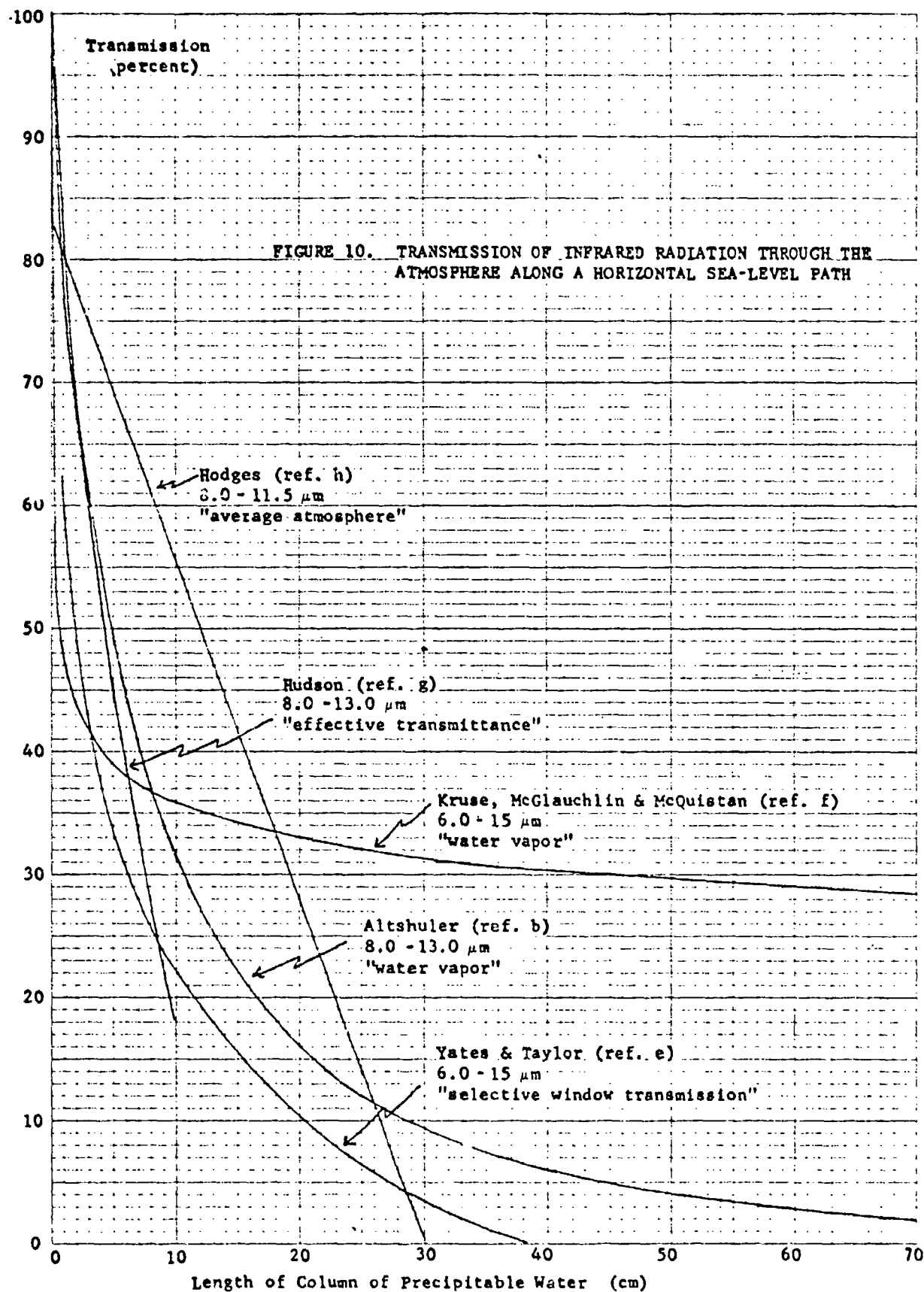
FIGURE 9. AVERAGE ATMOSPHERIC WATER VAPOR CONCENTRATION AS  
A FUNCTION OF ALTITUDE FOR EASTERN UNITED STATES



EUGENE DIETZGEN CO.  
MADE IN U. S. A.

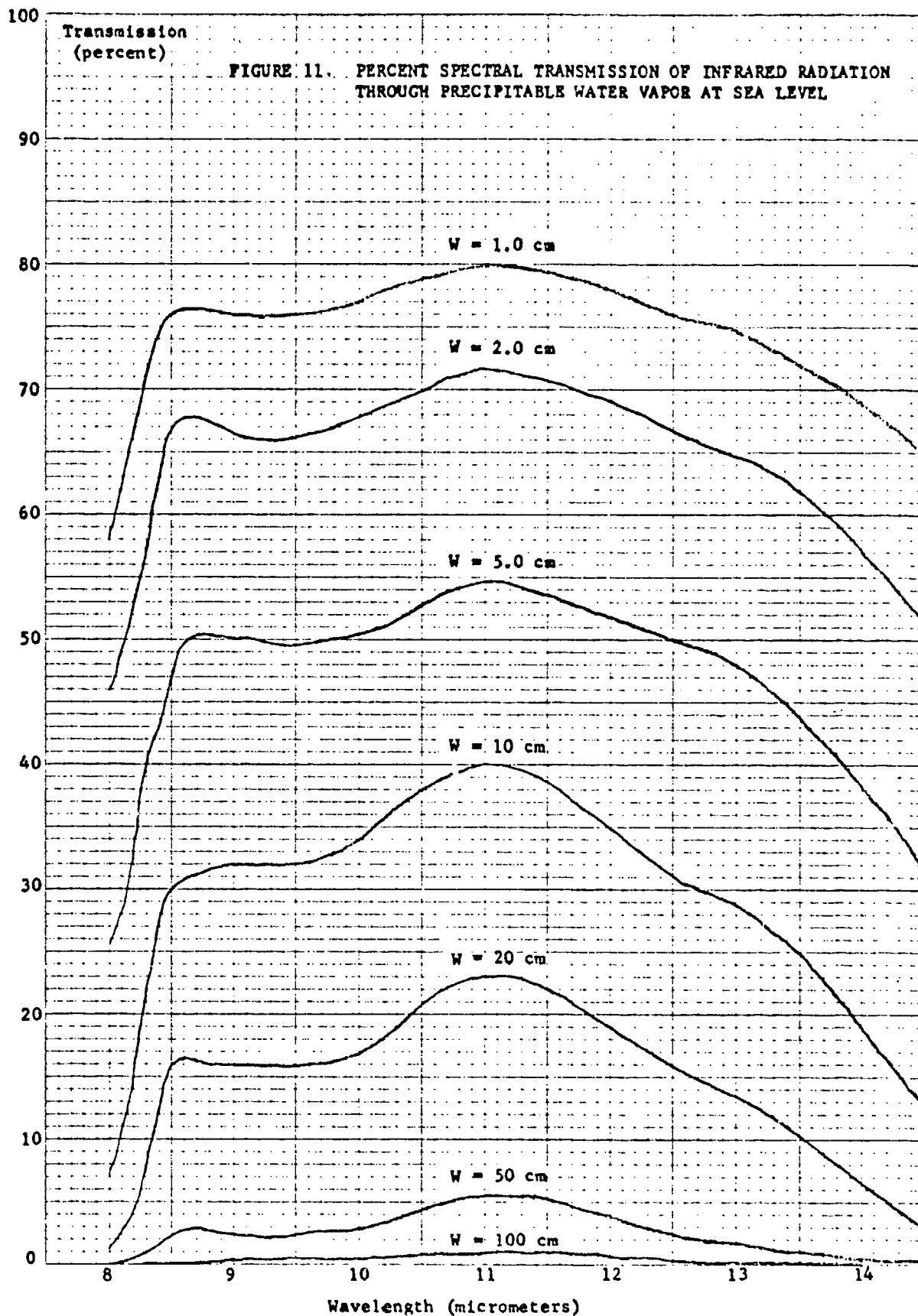
NO. 340-10 DIETZGEN GRAPH PAPER  
10 X 10 PER INCH

NO. 340-10 DIETZEN GRAPH PAPER  
10 X 10 PER INCH  
EUGENE DIETZEN CO.  
NEW YORK, N. Y.



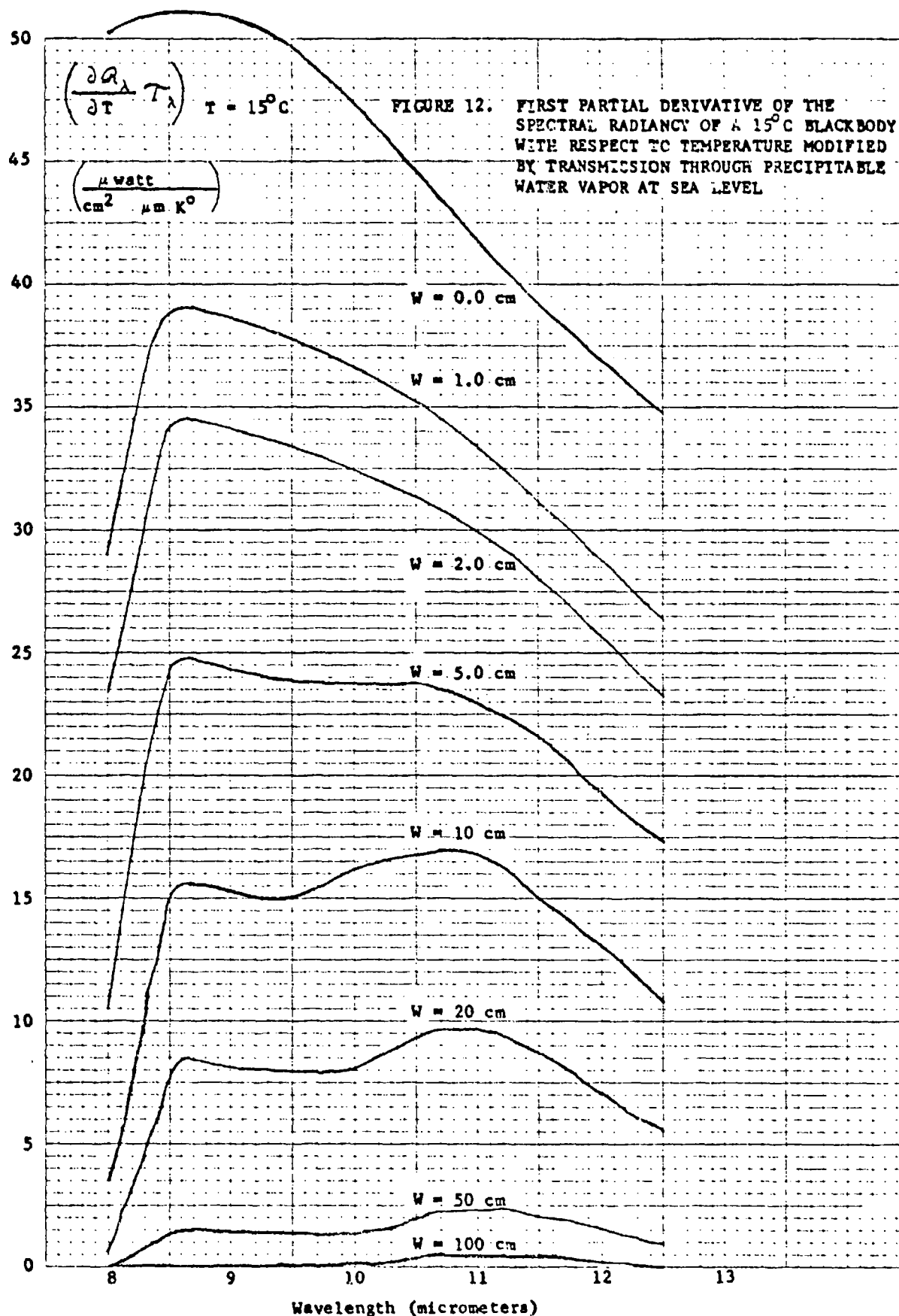
MADE IN U. S. A.

U. S. AIR FORCE



EUGENE DIETZGEN CO.  
MADE IN U. S. A.

NO. 3-10-10 DIETZGEN GRAPH PAPER  
10 X 10 PER INCH



CUBENE DIETZEN CO.  
MADE IN U. S. A.

NO. 340-10 DIETZEN GRAPH PAPER  
10 X 10 PER INCH

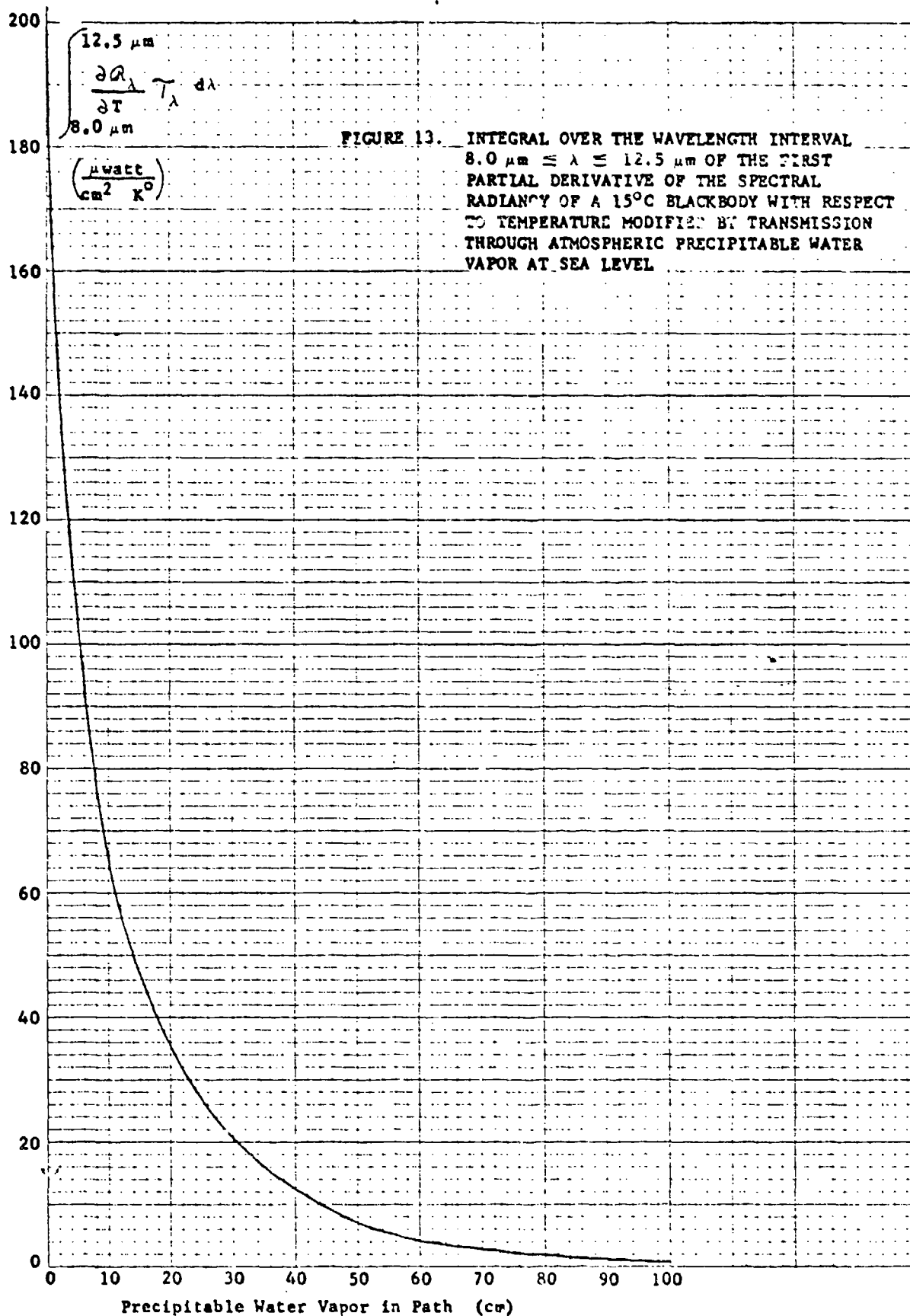
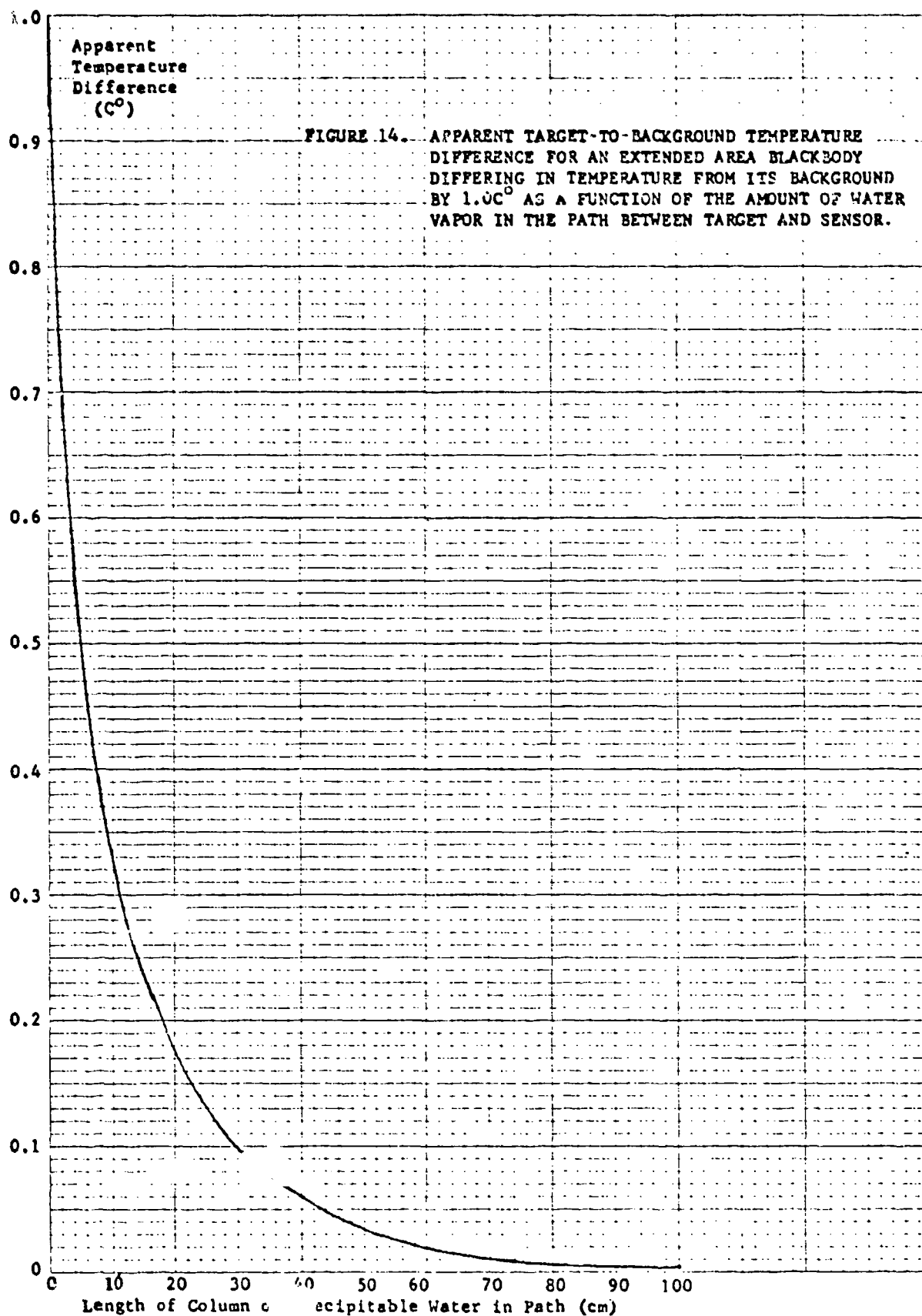


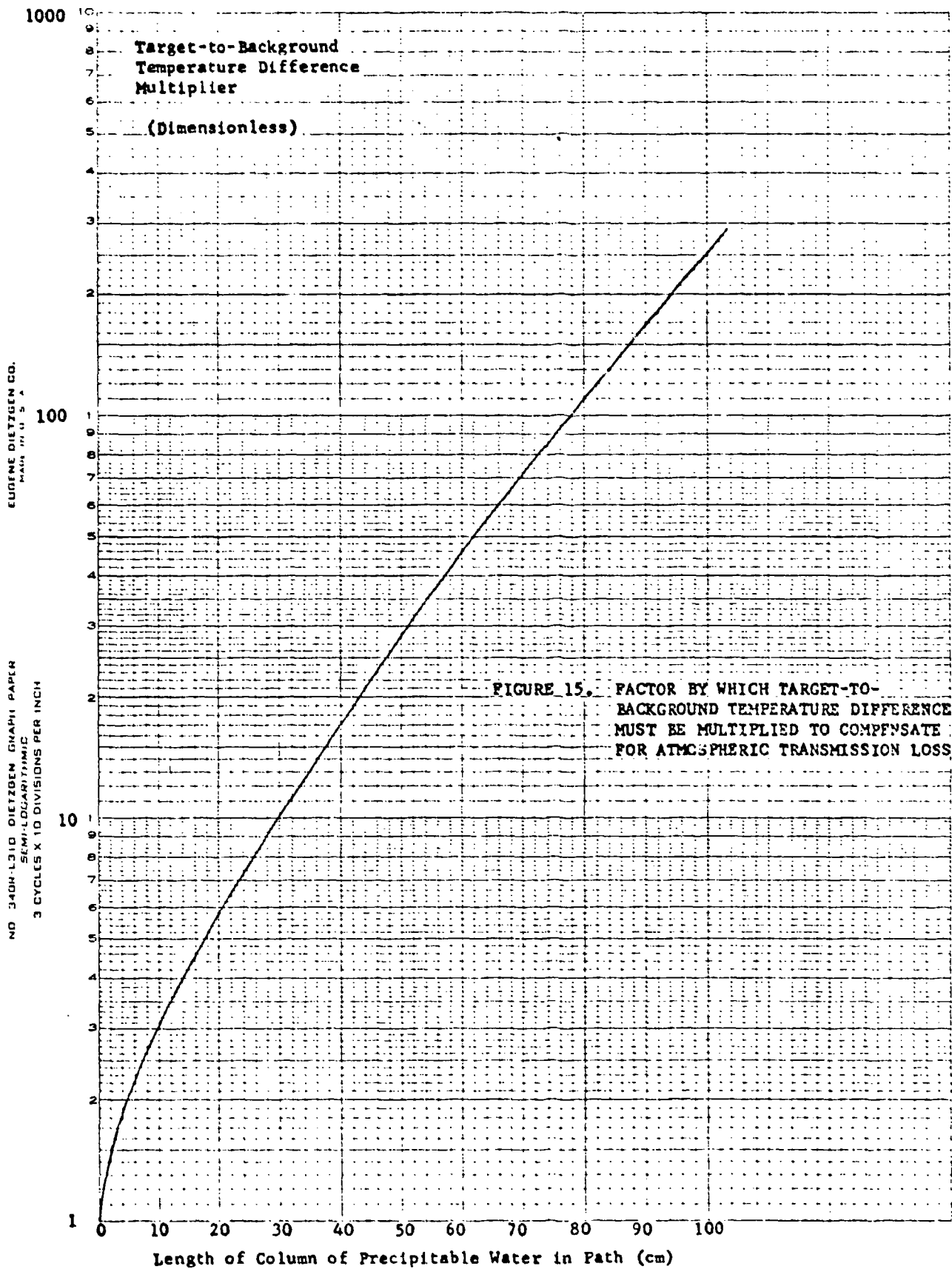
FIGURE 13. INTEGRAL OVER THE WAVELENGTH INTERVAL  $8.0 \mu\text{m} \leq \lambda \leq 12.5 \mu\text{m}$  OF THE FIRST PARTIAL DERIVATIVE OF THE SPECTRAL RADIANCE OF A  $15^\circ\text{C}$  BLACKBODY WITH RESPECT TO TEMPERATURE MODIFIED BY TRANSMISSION THROUGH ATMOSPHERIC PRECIPITABLE WATER VAPOR AT SEA LEVEL

EUDENE DIETZEN CO.  
MADE IN U. S. A.

NO. 340-10 DIETZEN GRAPH PAPER  
10 X 10 PER INCH







EUGENE DIETZGEN CO.  
MADE IN U.S.A.

NO. 340H-1310 DIETZGEN GRAPH PAPER  
SEMI-LOGARITHMIC  
3 CYCLES X 10 DIVISIONS PER INCH

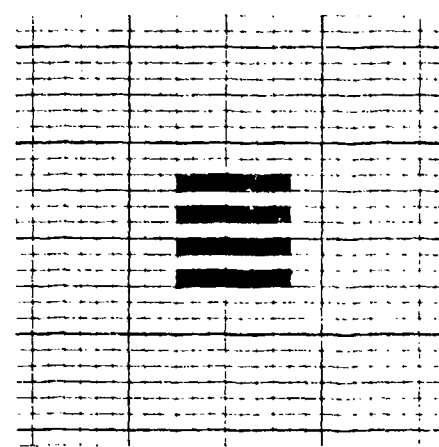
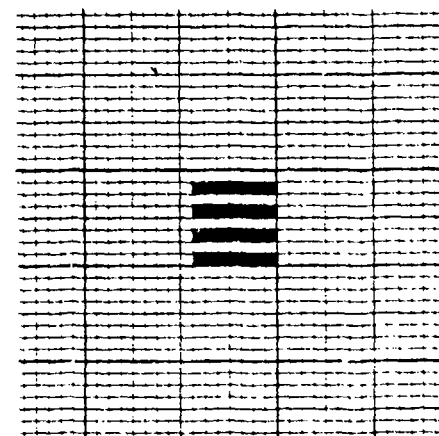
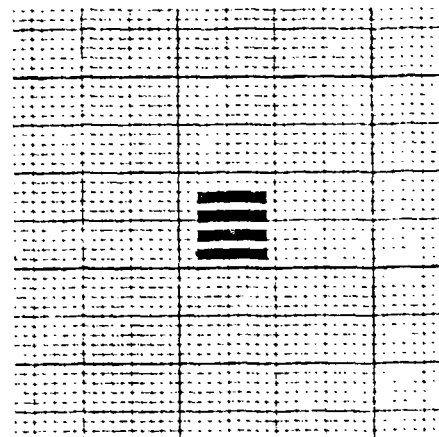
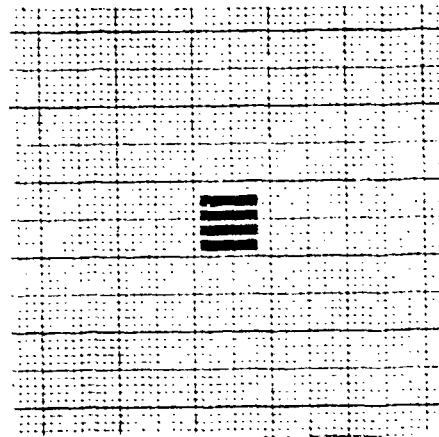
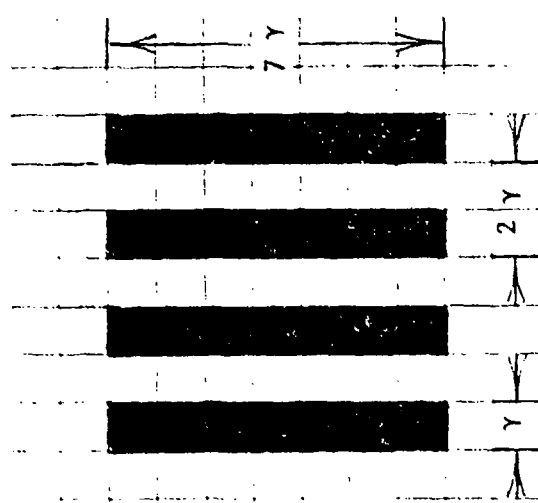
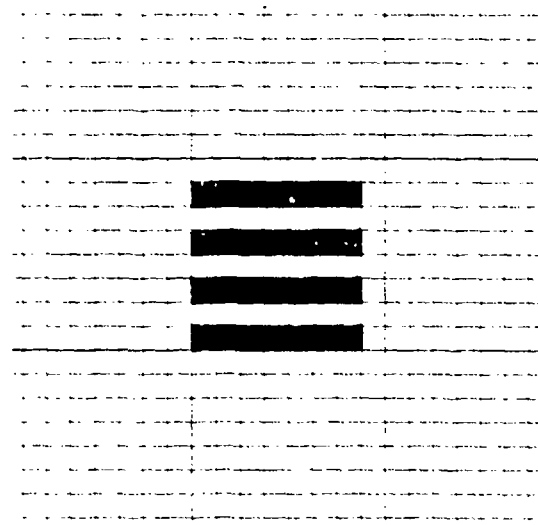
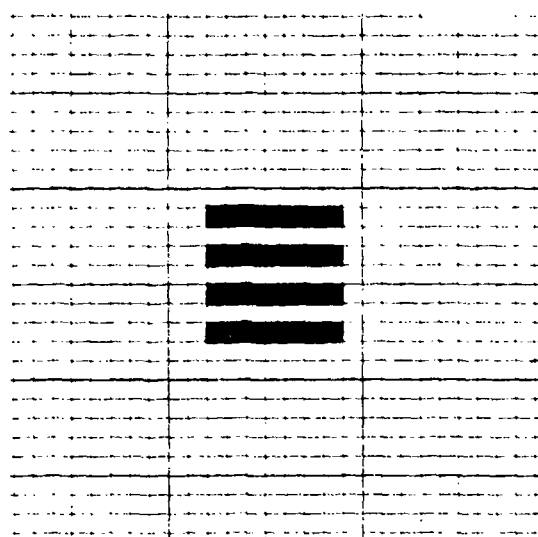
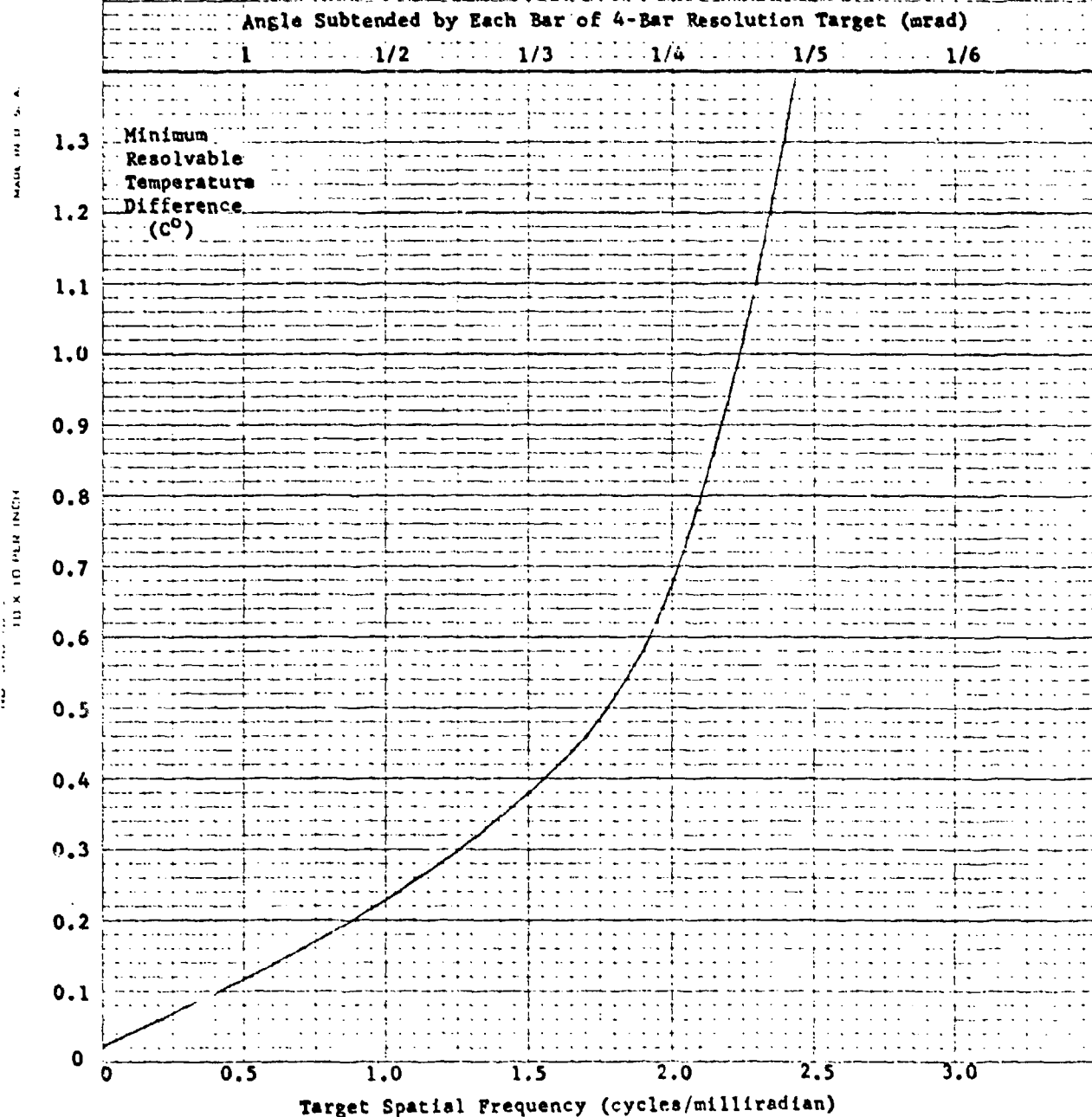


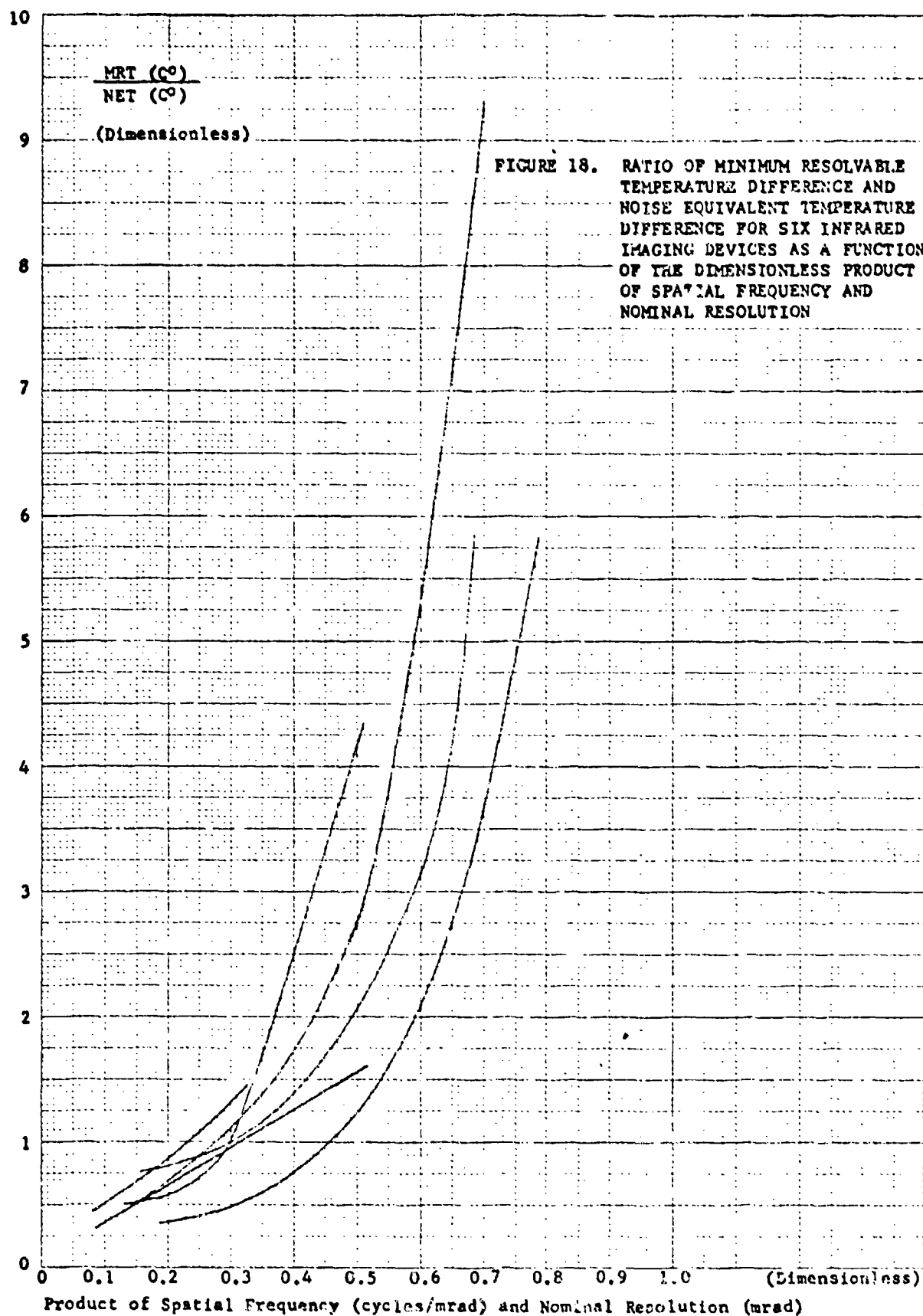
FIGURE 16. GEOMETRY OF FOUR-BAR TARGET ARRAY USED IN MRT DETERMINATION

FIGURE 17. REPRESENTATIVE MRT CURVE FOR A FLIR OF 0.25-MRAD NOMINAL RESOLUTION AND 0.25°C NOISE EQUIVALENT TEMPERATURE DIFFERENCE



EUGENE DIETZEN CO.  
MADE IN U.S.A.

NO. 3-10 20 DIETZEN GRAPH PAPER  
20 X 20 PER INCH



EUGENE DIETZEN CO.  
MADE IN U.S.A.

NO. 340 2D DIETZEN GRAPH PAPER  
5 1/2" X 20" PER INCH

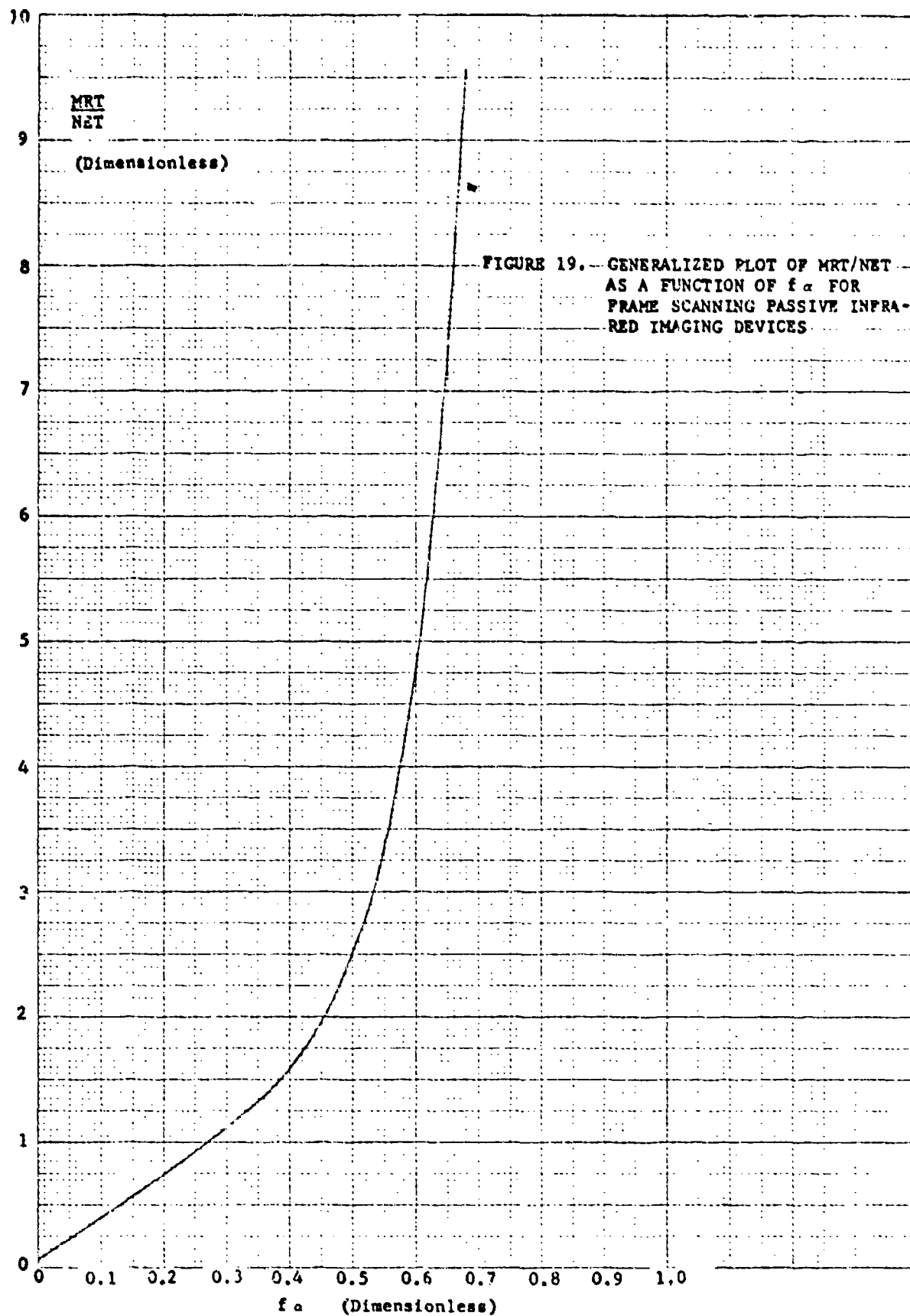
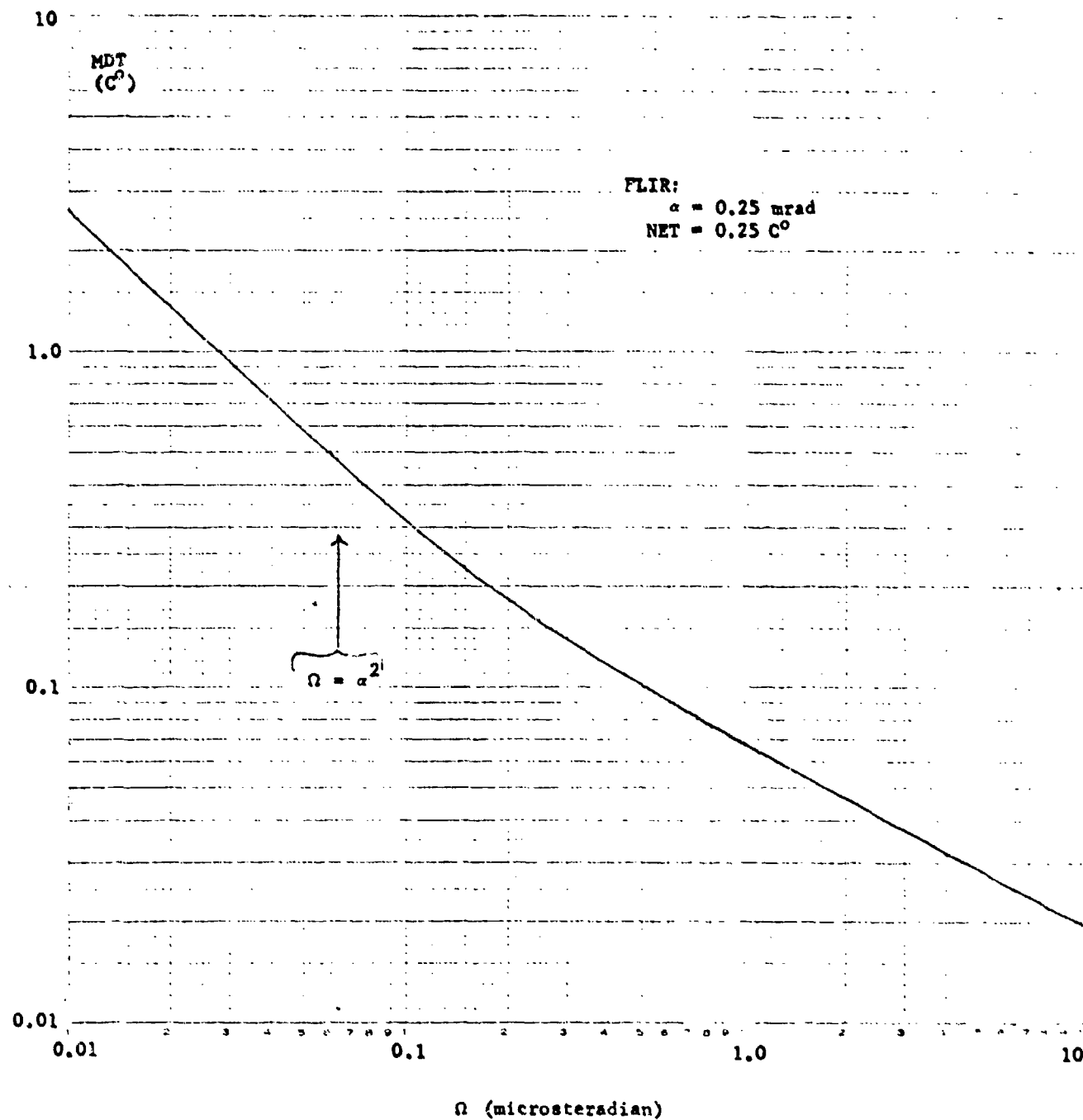


FIGURE 19. GENERALIZED PLOT OF MRT/NET  
AS A FUNCTION OF  $f_a$  FOR  
FRAME SCANNING PASSIVE INFRA-  
RED IMAGING DEVICES

FIGURE 20. MINIMUM DETECTABLE TEMPERATURE DIFFERENCE OF A REPRESENTATIVE FLIR AS A FUNCTION OF THE SOLID ANGLE SUBTENDED BY THE TARGET AT THE SENSOR



EUGENE DIETZEN CO.  
MADE IN U. S. A.

NO. 340-10 DIETZEN GRAPH PAPER  
10 X 10 PER INCH

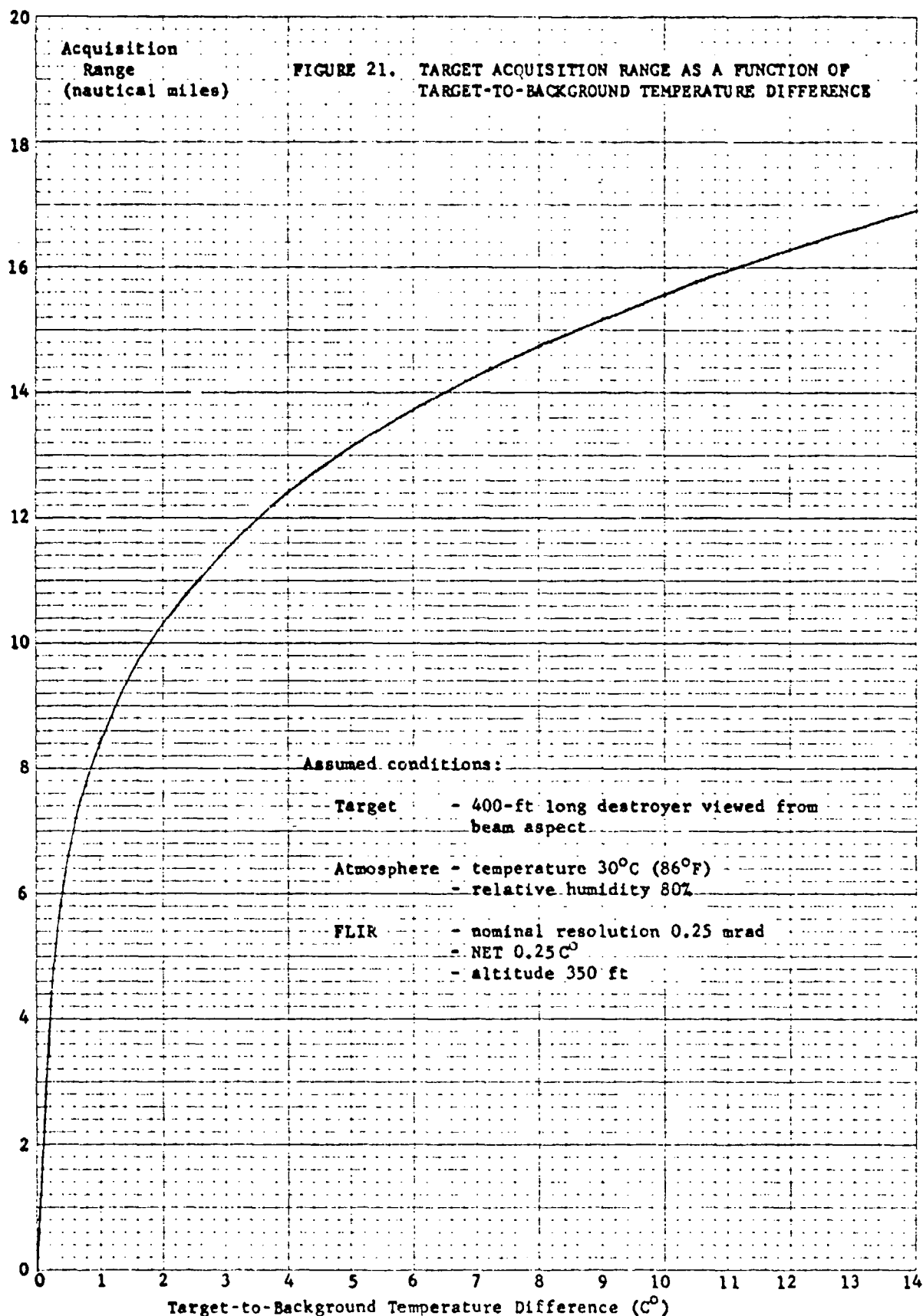
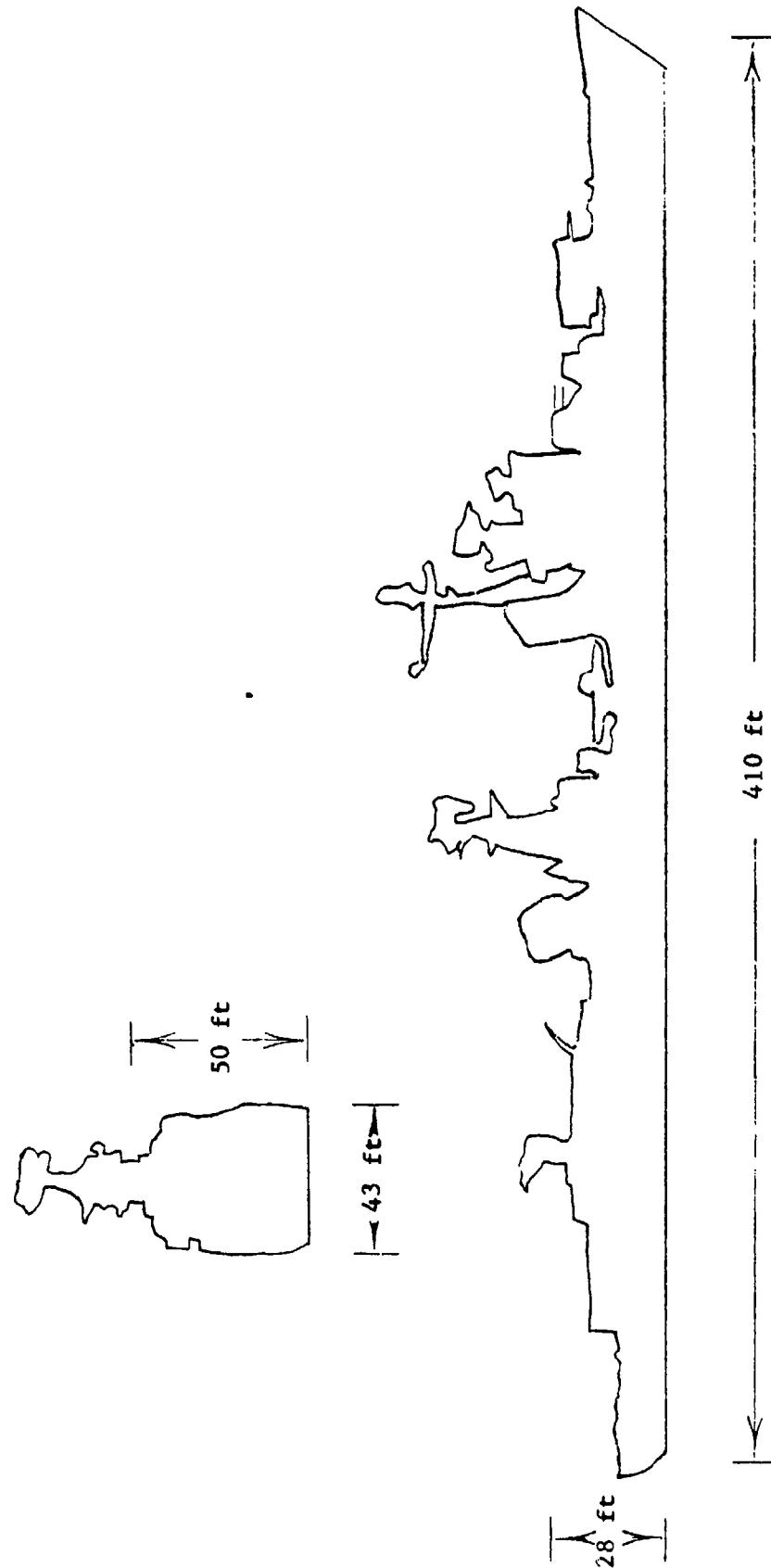


FIGURE 22. OUTLINE DRAWINGS OF A DESTROYER VIEWED  
FROM BOW AND BEAM ASPECT ANGLES





(a)

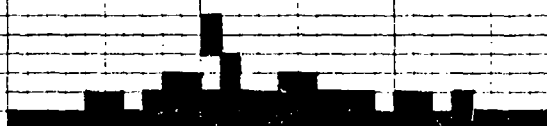


(b)



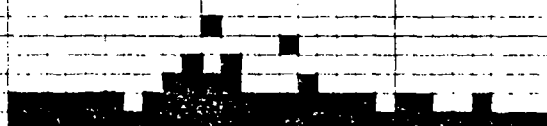
(63 blocks)

(c)



(53 blocks)

(d)



(58 blocks)

(e)

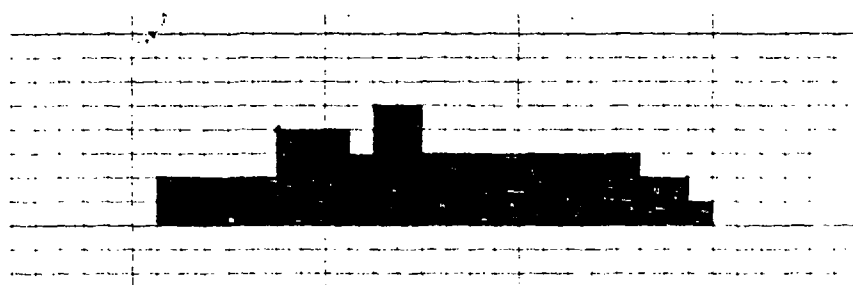


(64 blocks)

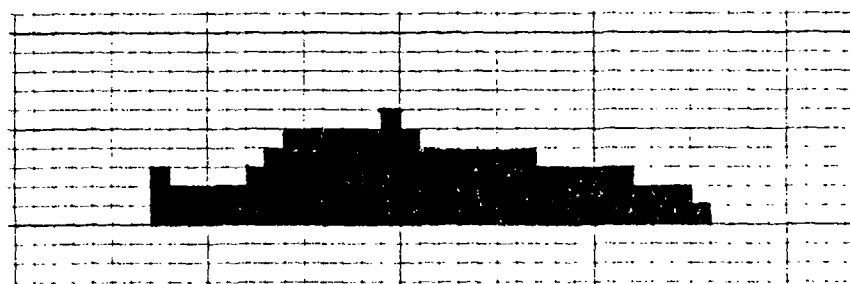
FIGURE 23. SILHOUETTE OF USS FORREST SHERMAN (DD 931) AND FOUR BLOCK SILHOUETTES OF THE SAME SHIP ILLUSTRATING QUANTIZING ERRORS



Ground resolution 32.8 ft  
(1.1 mrad at 5 nmi)  
14 blocks, 8 angles



Ground resolution 16.4 ft  
(0.54 mrad at 5 nmi)  
67 blocks, 16 angles



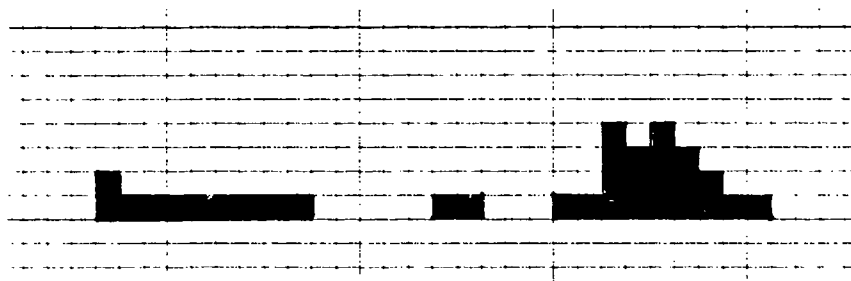
Ground resolution 13.1 ft  
(0.43 mrad at 5 nmi)  
100 blocks, 24 angles



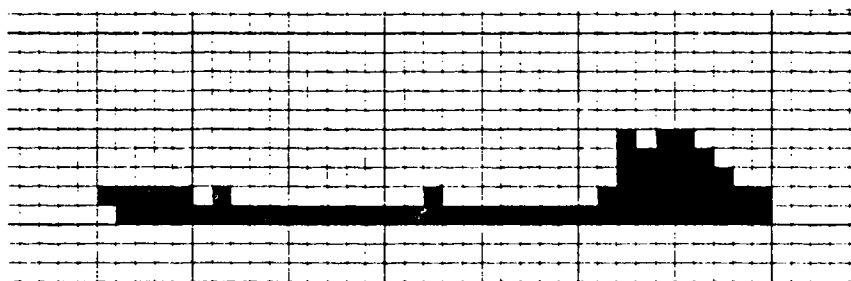
FIGURE 24. BLOCK-TYPE AND GRAPHIC PROFILE SILHOUETTES OF A SMALL PASSENGER SHIP (PRINCESS OF ACADIA). SCALE 131 FT/IN.



Ground resolution 32.8 ft  
(1.1 mrad at 5 nmi)  
8 blocks, 12 angles



Ground resolution 16.4 ft  
(0.54 mrad at 5 nmi)  
32 blocks, 26 angles



Ground resolution 13.1 ft  
(0.43 mrad at 5 nmi)  
64 blocks, 30 angles

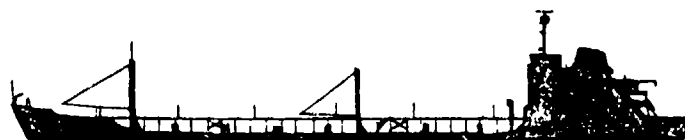
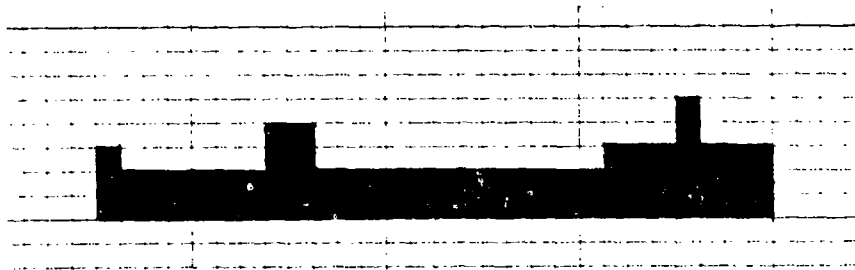


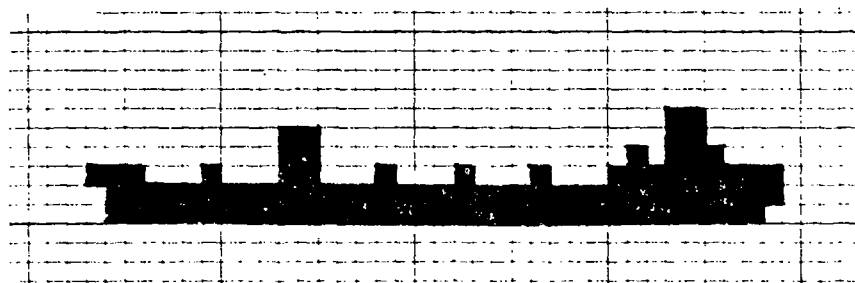
FIGURE 25. BLOCK-TYPE AND GRAPHIC PROFILE SILHOUETTES OF A SMALL TANKER (TAQUIPE). SCALE 131 FT/IN.



Ground resolution 32.8 ft  
(1.1 mrad at 5 nmi)  
16 blocks, 12 angles



Ground resolution 16.4 ft  
(0.54 mrad at 5 nmi)  
70 blocks, 16 angles



Ground resolution 13.1 ft  
(0.43 mrad at 5 nmi)  
99 blocks, 42 angles

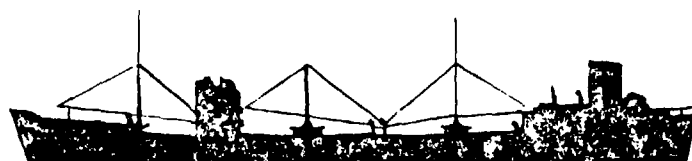
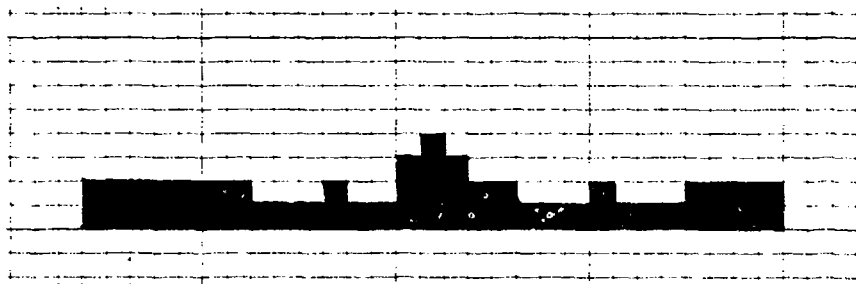


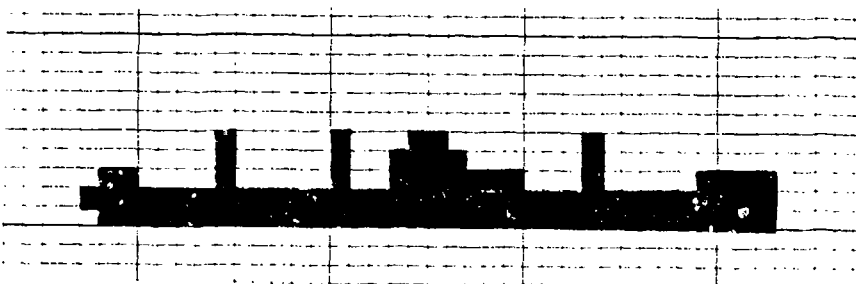
FIGURE 26. BLOCK-TYPE AND GRAPHIC PROFILE SILHOUETTES OF A FREIGHTER (HERA, MAJOY). SCALE 131 FT/IN.



Ground resolution 32.8 ft  
 (1.1 mrad at 5 nmi)  
 16 blocks, 8 angles



Ground resolution 16.4 ft  
 (0.54 mrad at 5 nmi)  
 51 blocks, 26 angles



Ground resolution 13.1 ft  
 (0.43 mrad at 5 nmi)  
 99 blocks, 34 angles

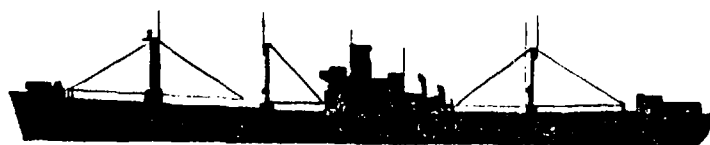
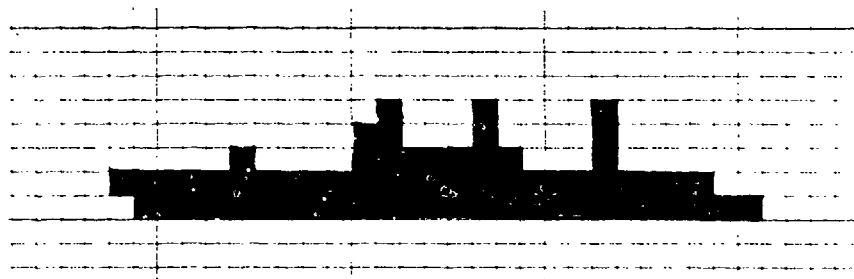


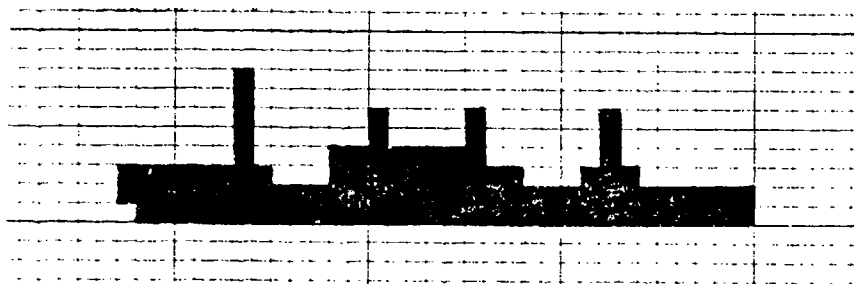
FIGURE 27. BLOCK-TYPE AND GRAPHIC PROFILE SILHOUETTES  
 OF A LIBERTY SHIP. SCALE 131 FT/IN.



Ground resolution 32.8 ft  
(1.1 mrad at 5 nmi)  
16 blocks, 12 angles



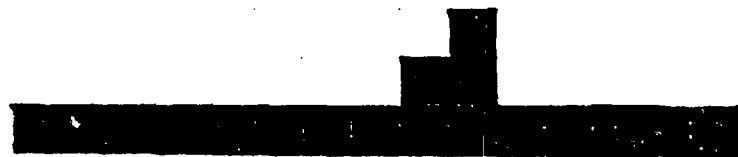
Ground resolution 16.4 ft  
(0.54 mrad at 5 nmi)  
67 blocks, 28 angles



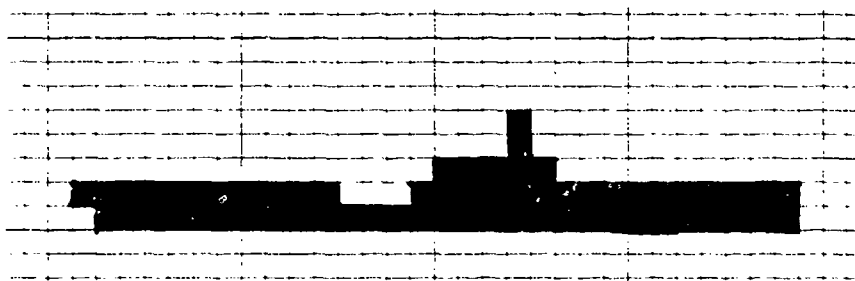
Ground resolution 13.1 ft  
(0.43 mrad at 5 nmi)  
106 blocks, 32 angles



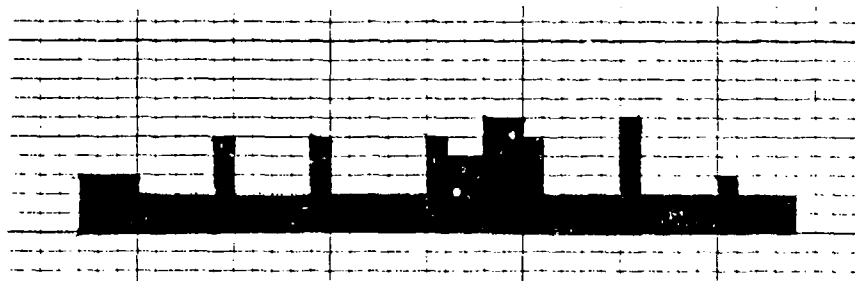
FIGURE 28. BLOCK-TYPE AND GRAPHIC PROFILE SILHOUETTES OF  
A CARGO VESSEL (ARTEMIS). SCALE 131 FT/IN.



Ground resolution 32.8 ft  
(1.1 mrad at 5 nmi)  
18 blocks, 10 angles



Ground resolution 16.4 ft  
(0.54 mrad at 5 nmi)  
63 blocks, 18 angles



Ground resolution 13.1 ft  
(0.43 mrad at 5 nmi)  
106 blocks, 32 angles



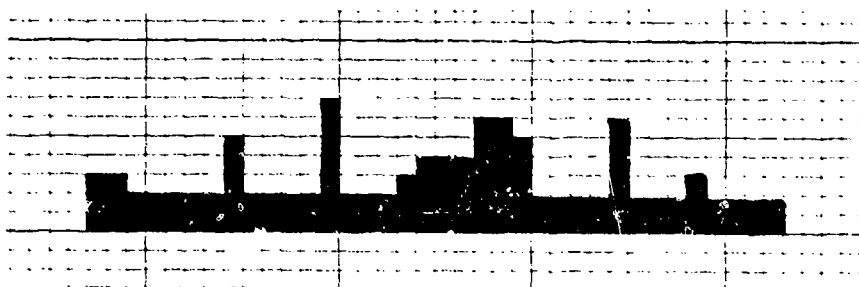
FIGURE 29. BLOCK-TYPE AND GRAPHIC PROFILE SILHOUETTES OF  
A CARGO VESSEL (RANGER), SCALE 131 FT/IN.



Ground resolution 32.8 ft  
(1.1 mrad at 5 nmi)  
16 blocks, 8 angles



Ground resolution 16.4 ft  
(0.54 mrad at 5 nmi)  
49 blocks, 30 angles



Ground resolution 13.1 ft  
(0.43 mrad at 5 nmi)  
105 blocks, 32 angles

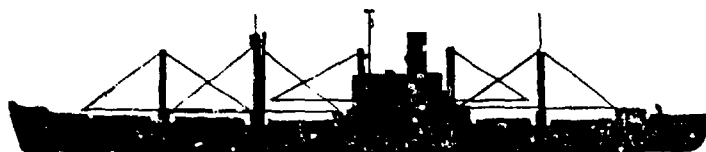
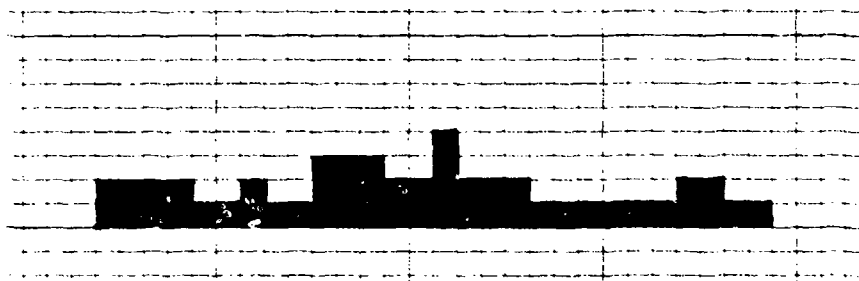


FIGURE 20. BLOCK-TYPE AND GRAPHIC PROFILE SILHOUETTES OF A CARGO VESSEL (ALCOA MARKETER). SCALE 131 FT/IN.

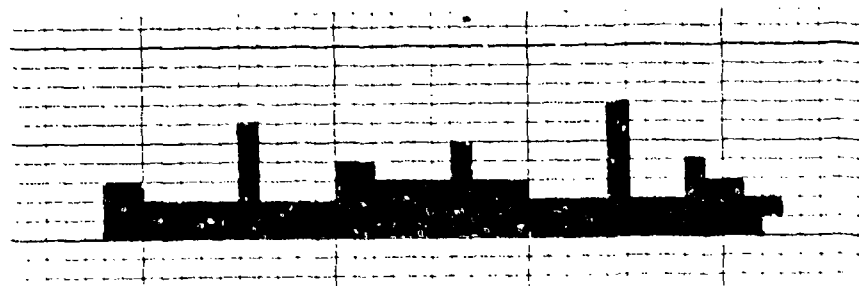




Ground resolution 32.8 ft  
(1.1 mrad at 5 nmi)  
16 blocks, 12 angles



Ground resolution 16.4 ft  
(0.54 mrad at 5 nmi)  
49 blocks, 24 angles



Ground resolution 13.1 ft  
(0.43 mrad at 5 nmi)  
95 blocks, 32 angles



FIGURE 31. BLOCK-TYPE AND GRAPHIC PROFILE SILHOUETTES OF  
A CARGO VESSEL (NIKOLAYEV). SCALE 131 FT/IN.

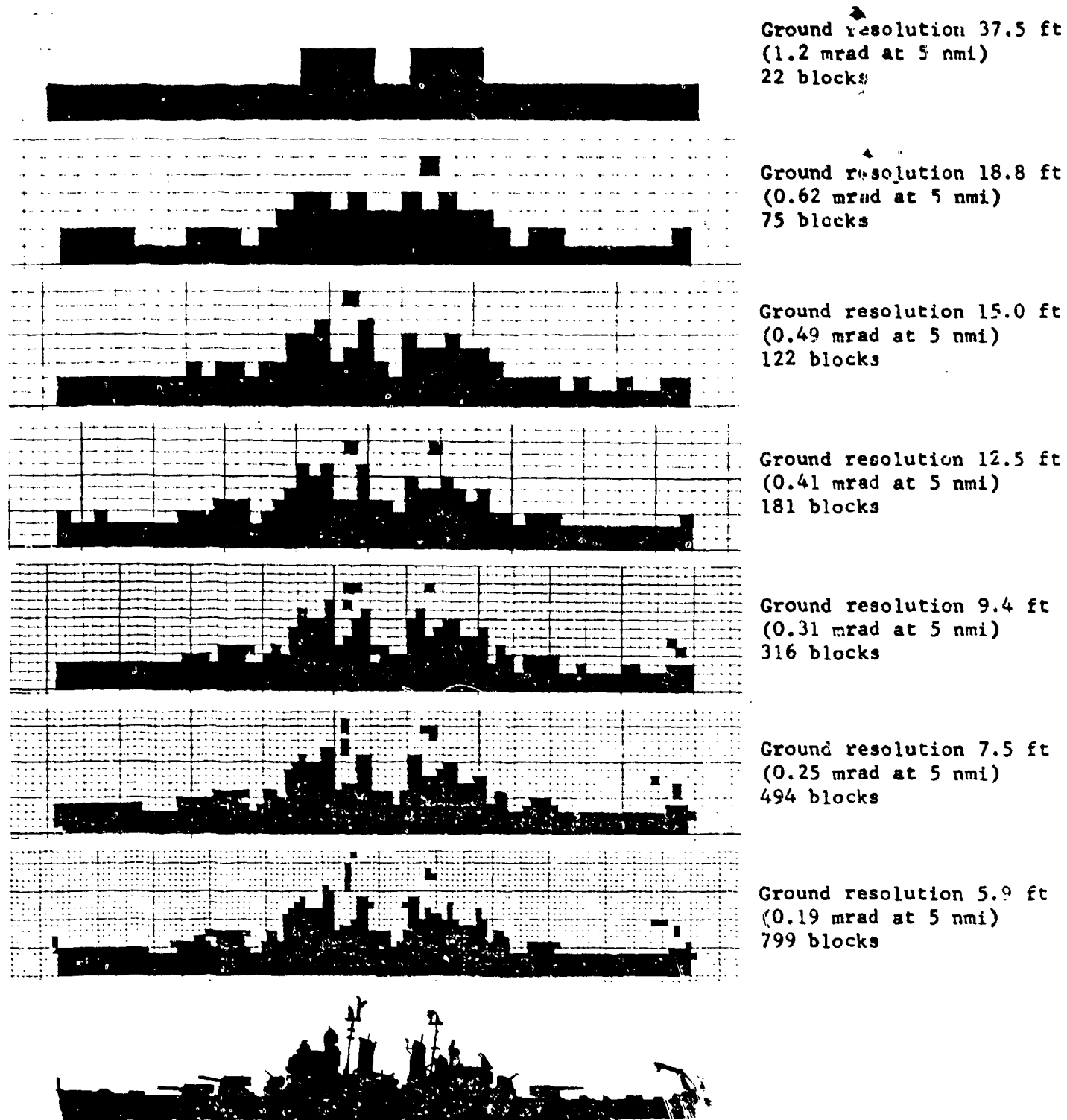


FIGURE 32. BLOCK-TYPE AND GRAPHIC PROFILE SILHOUETTES OF A BALTIMORE CLASS HEAVY CRUISER. SCALE 150 FT/IN.

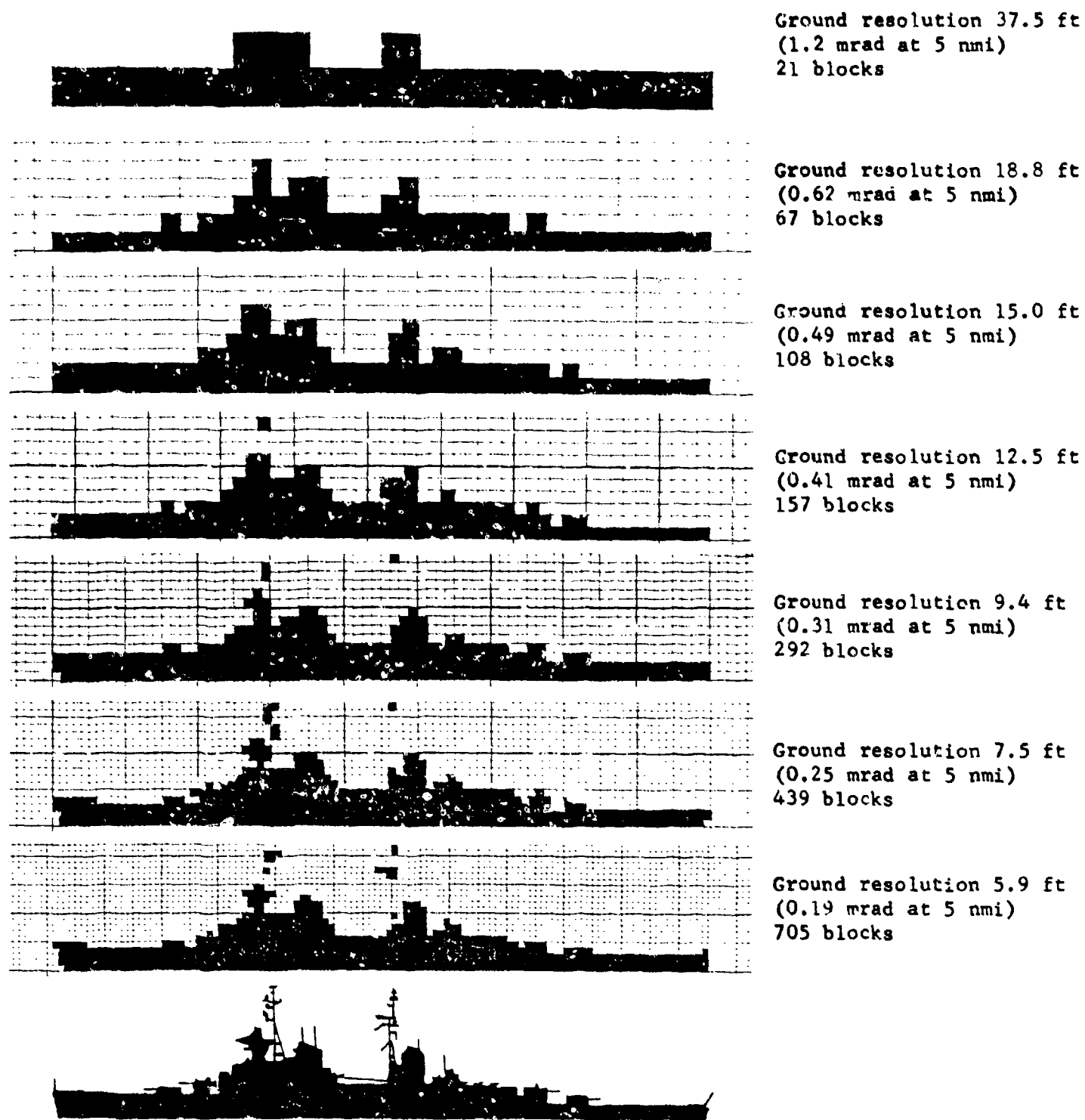


FIGURE 33. BLOCK-TYPE AND GRAPHIC PROFILE SILHOUETTES OF A SVERDLOV CLASS CRUISER. SCALE 150 FT/IN.

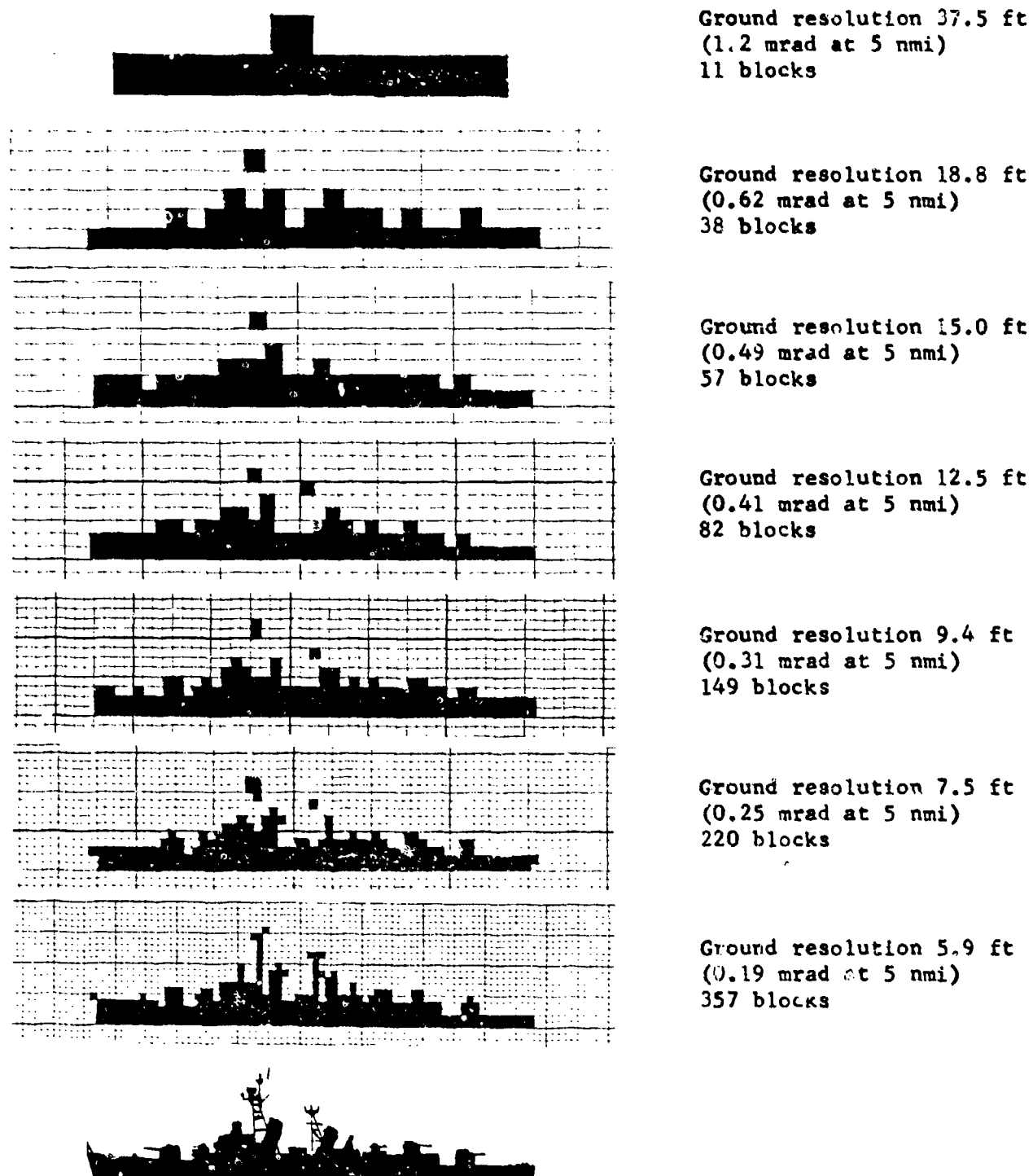
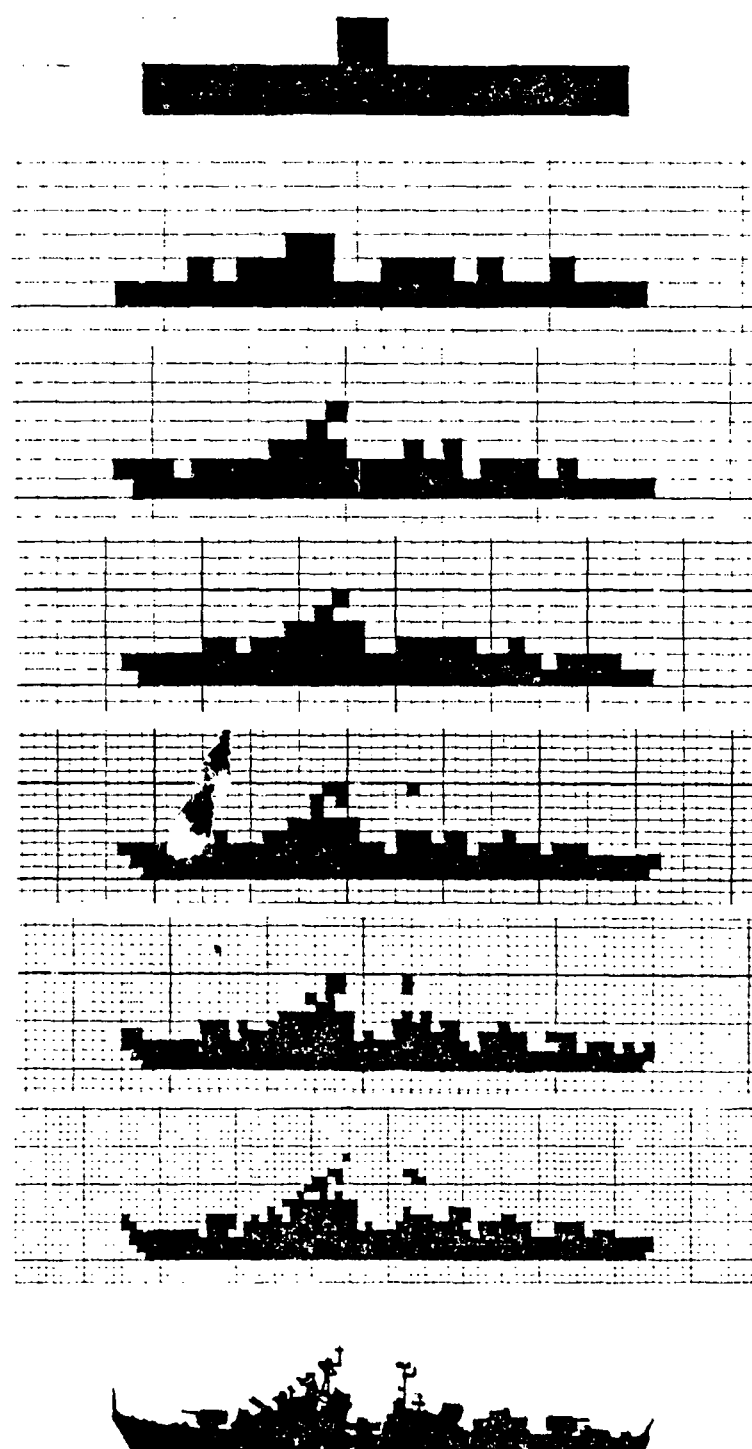


FIGURE 34. BLOCK-TYPE AND GRAPHIC PROFILE SILHOUETTES OF A FORREST SHERMAN CLASS DESTROYER. SCALE 150 FT/IN.



Ground resolution 37.5 ft  
(1.2 mrad at 5 nmi)  
11 blocks

Ground resolution 18.8 ft  
(0.62 mrad at 5 nmi)  
34 blocks

Ground resolution 15.0 ft  
(0.49 mrad at 5 nmi)  
56 blocks

Ground resolution 12.5 ft  
(0.41 mrad at 5 nmi)  
84 blocks

Ground resolution 9.4 ft  
(0.31 mrad at 5 nmi)  
146 blocks

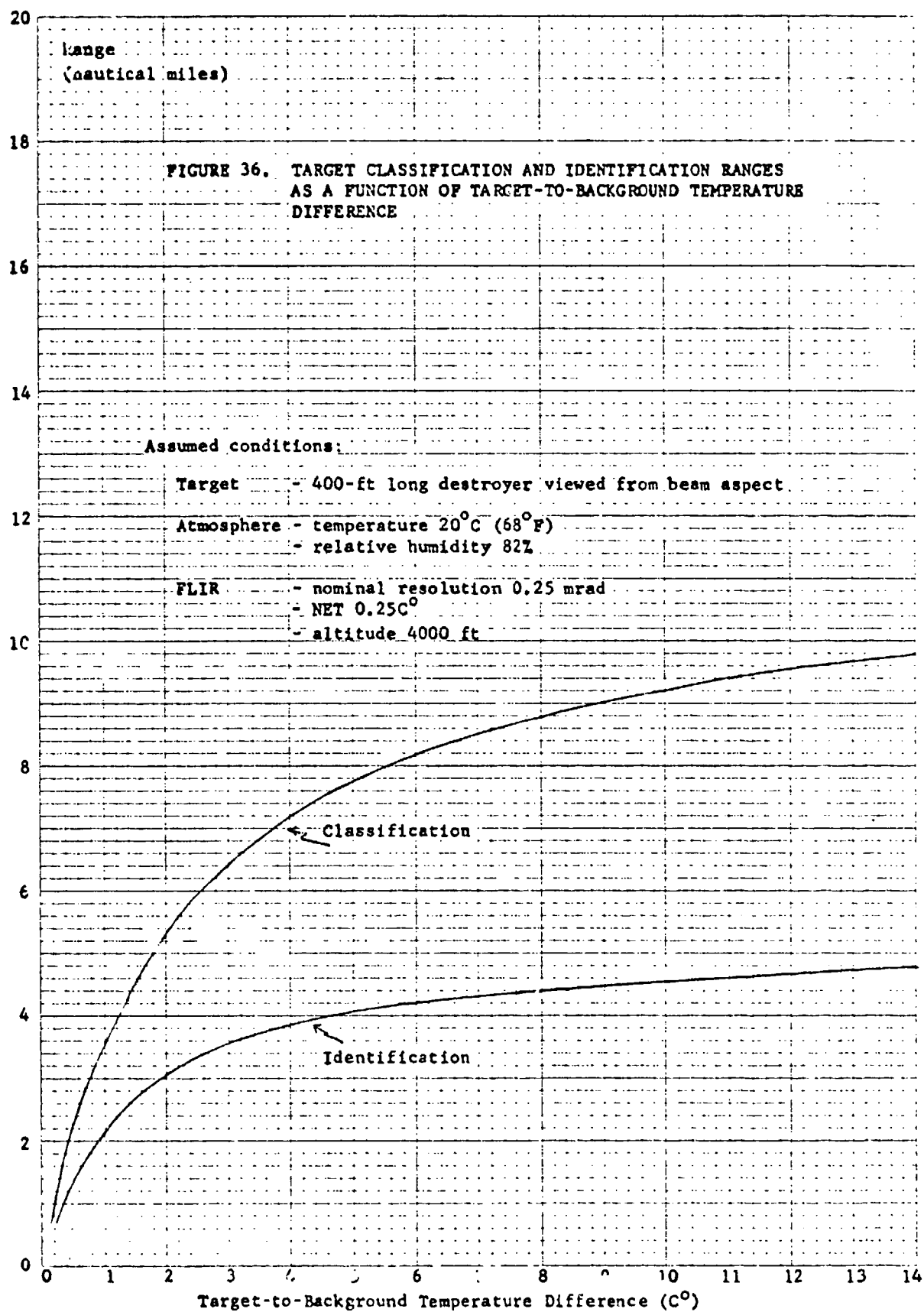
Ground resolution 7.5 ft  
(0.25 mrad at 5 nmi)  
227 blocks

Ground resolution 5.9 ft  
(0.19 mrad at 5 nmi)  
367 blocks

FIGURE 35. BLOCK-TYPE AND GRAPHIC PROFILE SILHOUETTES OF A KOTLIN CLASS DESTROYER. SCALE 150 FT/IN.

EUGENE DIETZGEN CO.  
MADE IN U. S. A.

NO. 340-110 DIETZGEN GRAPH PAPER  
10 X 10 PER INCH



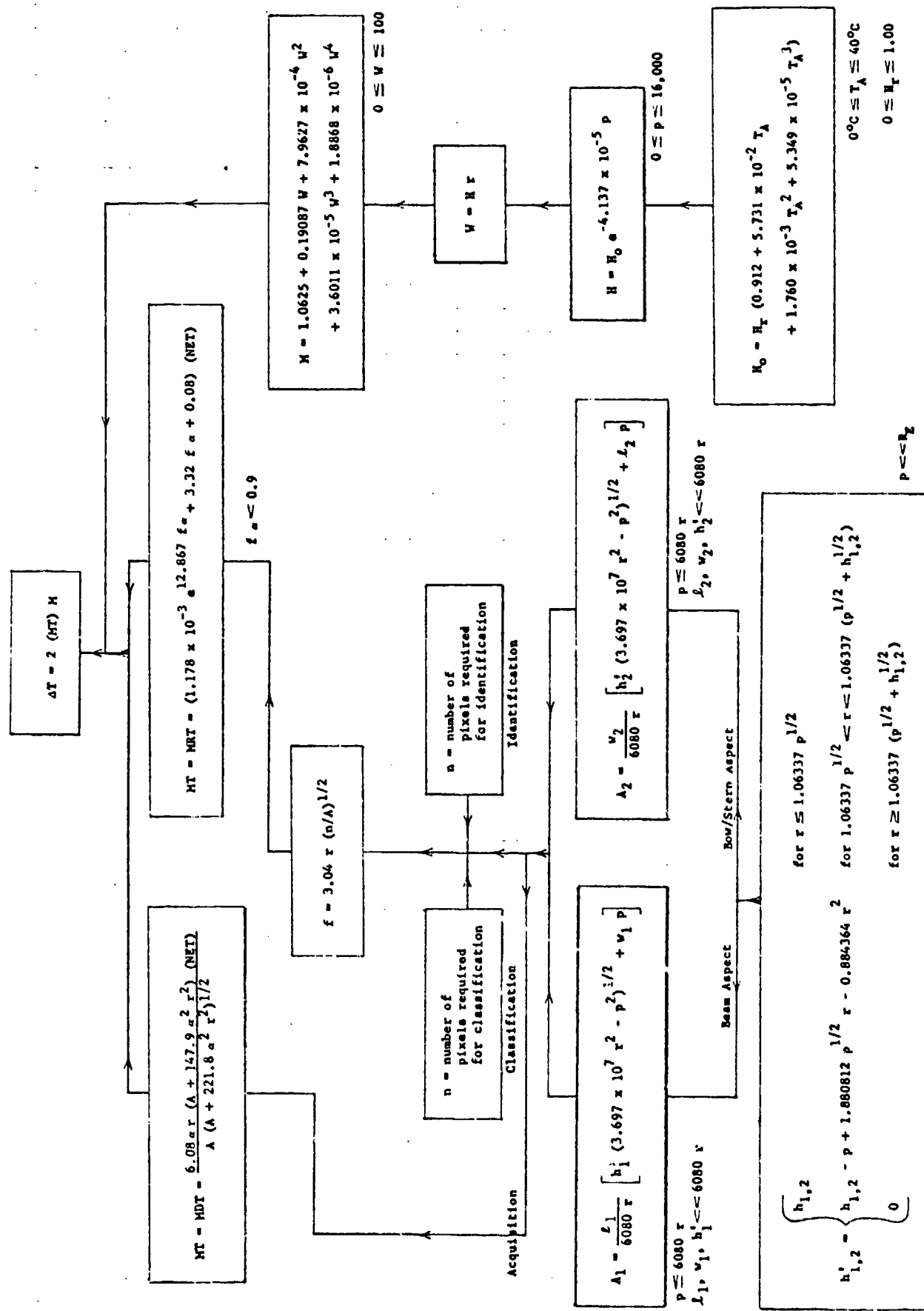


FIGURE 37. TARGET-TO-BACKGROUND TEMPERATURE DIFFERENCES REQUIRED TO PERMIT ACQUISITION, CLASSIFICATION AND IDENTIFICATION OF SHIPS BY AIRBORNE PASSIVE FLIR (FORWARD LOOKING INFRARED) IMAGING DEVICES